



HAL
open science

Spray behaviour from non-swirling to swirling gas jet in coaxial atomisation

Santanu Kumar Sahoo, Yu Wei, Nathanaël Machicoane

► **To cite this version:**

Santanu Kumar Sahoo, Yu Wei, Nathanaël Machicoane. Spray behaviour from non-swirling to swirling gas jet in coaxial atomisation. *Journal of Fluid Mechanics*, 2025, 1025, pp.A7. <10.1017/jfm.2025.10924>. <hal-05536422>

HAL Id: hal-05536422

<https://hal.science/hal-05536422v1>

Submitted on 5 Mar 2026

HAL is a multi-disciplinary open access archive for the deposit and dissemination of scientific research documents, whether they are published or not. The documents may come from teaching and research institutions in France or abroad, or from public or private research centers.

L'archive ouverte pluridisciplinaire HAL, est destinée au dépôt et à la diffusion de documents scientifiques de niveau recherche, publiés ou non, émanant des établissements d'enseignement et de recherche français ou étrangers, des laboratoires publics ou privés.



Distributed under a Creative Commons CC BY 4.0 - Attribution - International License

Banner appropriate to article type will appear here in typeset article

1 **Spray behavior from non-swirling to swirling gas jet** 2 **in coaxial atomization**

3 **Santanu Kumar Sahoo¹†, Yu Wei¹ and Nathanaël Machicoane¹**

4 ¹Univ. Grenoble Alpes, CNRS, Grenoble INP, LEGI, 38000 Grenoble, France

5 (Received xx; revised xx; accepted xx)

6 The present study focuses on the influence of gas swirl on the spray behavior from a two-
7 fluid coaxial atomizer with high gas-to-liquid dynamic pressure ratios M by varying both the
8 liquid Reynolds number Re_l and the gas Weber number We_g . The investigations identify the
9 deviations of the carrier phase velocity fields, droplet distribution, and dispersion when swirl
10 is introduced to the gas phase compared to the non-swirling conditions. The changes in the
11 axial, radial, and tangential velocities of the continuous phase due to the introduction of swirl
12 are highlighted while retaining a self-similar behavior. The slip velocity of the large droplets
13 in swirling sprays is negative, unlike the known positive value for non-swirling sprays. The
14 shape of the radial profiles of the mean drop size is investigated along We_g , notably revealing
15 an inflection point for swirling sprays at high We_g values. A global assessment of the drop
16 size uncovered that swirl leads to its increase for low M while assisting spray formation
17 at high M . Additionally, the radial profiles of axial fluxes for swirling sprays have a wider
18 bell-shaped curve compared to non-swirling sprays at high M , unlike the off-center maxima
19 found for low M . However, the mentioned dependencies of drop sizes and fluxes cannot be
20 determined by M solely for intermediate gas-to-liquid momentum ratios ($23 < M < 46$), and
21 vary with Re_l and We_g . In addition, the response of at least the mean droplets at the edge of
22 the spray to the large gas eddies shows a linear relation with swirl intensity.

23 **Key words:** multiphase flow, swirling gas jet, sprays, coaxial atomization

24 **1. Introduction**

25 Sprays, a collection of poly-disperse droplets, have wide applications at various scales that
26 include fuel spray production for combustion in different engines (Hardalupas *et al.* 1990;
27 Singh *et al.* 2020), targeted drug delivery in biological flows (Gürzing *et al.* 2022), metal
28 powder production for additive manufacturing (Ünal 1989; Qaddah *et al.* 2024), cleaning in
29 the semiconductor industry (Lallart *et al.* 2024), agricultural sprays (Makhnenko *et al.* 2021),
30 cooling for various applications such as data centers (Kandasamy *et al.* 2022) and coating of
31 surfaces like in pharmaceutical industry (Muliadi & Sojka 2010). The recent investigations
32 span towards real-time feedback control of the spray features (Osuna-Orozco *et al.* 2019,
33 2020, 2022). Bulk liquid is fragmented to form droplets with tailored characteristic sizes,

† Email address for correspondence: nathanael.machicoane@univ-grenoble-alpes.fr

34 distributions, and associated velocities tailored for these applications. One of the commonly
 35 used methods relies on high pressure liquid ejection, resulting in shear-driven hydrodynamic
 36 instability of high-velocity bulk liquid to form droplets. In most practical applications, this
 37 method is accompanied by an assisted air stream that further enhances the instabilities and
 38 leads to an augmented droplet formation process (Dumouchel 2008). In such cases, the
 39 fundamental mechanism driving the enhanced break up of the bulk liquid is an increase in
 40 stresses (Lasheras & Hopfinger 2000). With a view to further contribute to the existing stresses
 41 for droplet generation and modify the dispersion, an accompanied tangential component can
 42 be employed by the introduction of swirling motion to the gas jet (Hardalupas & Whitelaw
 43 1994; Hopfinger & Lasheras 1996). We investigate such a configuration here.

44 In single phase already, the high-momentum round jet has rich dynamics. Some of the
 45 key features include near orifice Kelvin-Helmholtz (K-H) instabilities (Crow & Champagne
 46 1971), a potential core (Ko & Davies 1971), a universal spread-rate of ≈ 0.1 (Panchapakesan
 47 & Lumley 1993; Pope 2001), self-similar velocity behavior (Hussein *et al.* 1994), entrainment
 48 (Liepmann & Gharib 1992) and helical modes away from the nozzle (Takahashi *et al.* 2023).
 49 Furthermore, the outer shear layer formed from the jet constitutes growing vortices whose
 50 convection velocity is given by (Dimotakis *et al.* 1983)

$$51 \quad U_c = \frac{\sqrt{\rho_1}U_1 + \sqrt{\rho_2}U_2}{\sqrt{\rho_1} + \sqrt{\rho_2}}, \quad (1.1)$$

52 where 1 and 2 represent two different fluid streams, here the fluid of the jet and the fluid
 53 into which the jet is discharged. A similar behavior is observed in the case of annular jets
 54 (Kuhlman 1987). In coaxial atomizers, a central round liquid jet is surrounded by an annular
 55 gas jet, which are typically, low and high momentum, respectively. Many of the gas jet features
 56 get altered due to the low momentum liquid at the center, and along with their transport, affect
 57 the spray generation process, the gas phase velocity, the droplet dynamics, and dispersion
 58 (Rehab *et al.* 1997; Favre-Marinet *et al.* 1999). Therefore, a coherent comparison in the gas jet
 59 Reynolds number of industrial relevance can be instrumental in characterizing the spray. In
 60 addition, when the gas swirl intensity is high, vortex breakdown is observed near the injector
 61 due to low pressure at the center of the jet (Billant *et al.* 1998), yet another feature that needs
 62 to be considered when investigating the spray in the presence of swirling gas configuration
 63 (Rajamanickam & Basu 2017). This high swirling flow essentially includes the presence of
 64 a stagnation point due to its imposition of adverse pressure gradient in the gas flow, resulting
 65 in a recirculation zone with a central core (Oberleithner *et al.* 2011; Rajamanickam & Basu
 66 2018).

67 Investigations on the influence of gas swirl on sprays have spanned many flow configura-
 68 tions. For example, Ade *et al.* (2023) investigated the influence of swirling gas on the breakup
 69 of a single droplet and found that, under high swirling conditions, finer satellite droplets are
 70 formed. Such an influence of the swirl is also observed by Rostami *et al.* (2025) for droplets
 71 with a wide range of velocities in a spray from a pressure-swirl atomizer introduced into
 72 a swirling coflow. In addition, Rostami *et al.* (2024) addressed the influence of coflowing
 73 swirling air on large-Stokes-number sprays and showed that swirl affects the important length
 74 scales of clusters, the number density of droplets in those clusters, and the most probable drop
 75 size in different clusters. In coaxial atomization, in addition to such droplet and swirled-flow
 76 interactions, the angular momentum imparted to the gas jet plays a role in the spray formation
 77 mechanisms, as well as in the droplet dispersion and breakup/coalescence balance further
 78 downstream.

79 The spray formation mechanism in a coaxial atomizer entails a sequence of processes
 80 (Lasheras & Hopfinger 2000). As the liquid and gas phases come in contact near the atomizer,

81 the shear instability is developed and leads to the formation of interfacial waves on the liquid
 82 jet (Marmottant & Villermaux 2004; Matas *et al.* 2018). At low gas momentum conditions,
 83 the asymmetric nature of these waves with gradual downstream progression leads to the
 84 flapping instability where the jet meanders radially (Delon *et al.* 2018). The liquid jet's shape
 85 formed by the flapping instability promotes the formation of membranes, where the liquid is
 86 first flattened, then inflated into a bag with a thin film and a thicker rim, a regime of shear
 87 breakup referred to as bag breakup. With supporting numerical (Zandian *et al.* 2018; Ling
 88 *et al.* 2019) and experimental (Lozano & Barreras 2001; Delon *et al.* 2018) investigations, it
 89 is established that the flapping of the liquid jet is due to the formation of local recirculation
 90 zones in the wake of the jet, leading to alternating low-pressure and high-pressure zones.
 91 Alternatively, at high We_g , the interfacial perturbations stretch to form ligaments that detach
 92 from the bulk liquid or may form droplets due to Rayleigh-Taylor instability with minimal
 93 large-scale movement (Lasheras & Hopfinger 2000), in what is called fiber-type atomization.
 94 The resultant morphology and the flow field resemble a backward-facing step where the fine
 95 droplets are at the edge, and the big ones are at the center (Huck *et al.* 2022). While the
 96 potential modifications of the nature of the instabilities of the liquid jet by swirl addition to
 97 the gas jet received little attention, their magnitudes and frequencies are observed to vary
 98 (Kumar & Sahu 2019; Machicoane *et al.* 2020).

99 In coaxial atomization, the central core in swirling gas flows makes the bulk liquid expand
 100 while breaking up (Hopfinger & Lasheras 1996; Dunand *et al.* 2005). As a result, although
 101 an apparent change in the spray evolution is observed by Préaux *et al.* (1998), it has not
 102 been explored in depth unlike the well-characterized non-swirling counterpart. For straight
 103 gas jets, it is reported that vortices generated by the K-H waves can influence the trajectory
 104 of droplets following their breakup. For example, in planar shear layers, the recirculation
 105 region formed downstream of these waves catapult the droplets to eject them at very high
 106 angles compared to the primary momentum direction (Jerome *et al.* 2013). Such high-angle
 107 ejections are also mentioned in coaxial atomization by Huck *et al.* (2022). While these
 108 observations are limited to low gas momentum conditions, at high momentum, other factors
 109 such as high-entrainment rates, the substantial dominance of the helical modes associated
 110 with the gas jet without or with swirl also plays a key role in the organization of the droplets
 111 (Dunand *et al.* 2005). Such features happen in parallel to the expected reduction in the spray
 112 drop size as the gas momentum (and kinetic energy) increases. This effect also comes with
 113 a reduction in the spray cone angle. Therefore, additional methods like swirl hold immense
 114 relevance, since gas swirl can mitigate or counteract the reduction in the spray dispersion.

115 Sustained high gas momentum following the breakup of droplets (as a very small fraction
 116 of the kinetic energy is contributing the formation of droplets (Yarin *et al.* 2017)) will drive
 117 the transport for the majority of the droplets. For the big droplets, though, which contribute
 118 significantly to the volumetric quantities like mass flux, the response to the gas flow is more
 119 complicated. Such flow investigations have close allegiance with the works on particle-laden
 120 jets (PLJs) due to the retaining of the droplet size far from the developing region and their
 121 sparse concentration in the carrier fluid. Undoubtedly this comparison does not apply to either
 122 the near-field breakup and the dense concentration region dynamics in particle-laden flows
 123 mentioned in the regime map of Brandt & Coletti (2022). The most important parameter for
 124 investigating these flows identifies the response of particles or droplets, ascertained by the
 125 ratio of their response time scale (τ_p) with respect to the carrier flow time scales (τ_f) called
 126 the Stokes number (Squires & Eaton 1990):

$$127 \quad St = \tau_p / \tau_f. \quad (1.2)$$

128 The general consensus in this regard is that particles perfectly follow the flow when $St < 0.01$,
 129 and do not respond when this value is greater than 10 (Balachandar & Eaton 2010). Particles

130 with $0.01 < St < 10$ are known to respond to the flow partially. Earlier investigations by
131 (Modarress *et al.* 1984; Hardalupas *et al.* 1989) examined these aspects and identified the
132 mechanisms for energy transfer between the dispersed and the continuous phase. With a
133 similar theme, the investigations by Longmire & Eaton (1992); Lazaro & Lasheras (1992)
134 investigated a shear layer with particles and reported about particle dispersion for $St =$
135 1. Apart from the significant focus on the clustering behavior of particles and droplets
136 (Angriman *et al.* 2022; Sahu *et al.* 2018; Manish & Sahu 2019), which is a consequence
137 of the interaction of carrier phase eddies with the droplets, additional factors determining
138 the particles' response to flow have been brought forward by recent investigations of Lau &
139 Nathan (2014, 2016). This includes linking the initial conditions to the reduced dispersion
140 of particles with increasing Stokes number in the far field of the PLJs. This analysis pointed
141 to an interesting competition between the Saffman force acting on the high Stokes number
142 particles to bring them to the centerline and turbophoresis acting on particles with small St
143 to accumulate them near the edges when investigated dispersion near the exit of the jet. The
144 investigations on dispersion presented earlier by Hardalupas & Whitelaw (1994), recently
145 by Huck *et al.* (2022) for non-swirling sprays and more recently by Fong *et al.* (2024) for
146 swirling sprays unify the commonalities but are far from exhaustive to fully understand the
147 dispersion of droplets in sprays, especially in the presence of gas swirl.

148 Numerous investigations over many decades have focused significantly on the instabilities
149 in the liquid jet leading to its breakup (Marmottant & Villermaux 2004; Matas *et al.* 2018;
150 Kumar & Sahu 2019). Despite the realization that the downstream evolution of droplets
151 cannot be easily related to the upstream breakup regimes, there are very few assessments for
152 the former. To make these investigations relevant, diverse fluid dynamic quantities must be
153 determined. For example, it is essential from the perspective of applications to understand the
154 gas flow properties that can influence momentum transport. In reacting systems, the carrier
155 phase also determines energy transfer (Gounder *et al.* 2012). For such analyses, there is a
156 scarce presence of investigations with physically relevant quantities in the context of sprays.
157 With increased realization of the benefits of swirling environment in combustion applications
158 (Hoffmann *et al.* 1997; Kwarck *et al.* 2005) and metal powder production (Qaddah *et al.* 2024),
159 it is pertinent to make such investigations for swirling sprays. Although recent advancements
160 in this regard have shed new light, the applicability is limited to only a narrow parameter
161 range. These considerations severely undermine the significant differences in the breakup
162 behavior near the atomizer and the existing understanding of their relation as the droplets
163 travel downstream. Additionally, the response of large droplets in the carrier phase, which
164 can be instrumental in applying the understanding of the particle-laden jets for modeling, is
165 almost negligible in the literature in the case of swirling sprays.

166 Therefore, the present investigation addresses these gaps in the literature on swirling sprays.
167 The experimental details are described in Section 2. An overview of the spray generation
168 mechanisms is provided in Section 3. We follow it up with the investigations of the kinematics
169 of the swirling flow in Section 4. A comprehensive droplet size analysis is presented in Section
170 5, which is followed by the results on spray dispersion in Section 6. We close the findings of
171 this article with a discussion and conclusion (Section 7).

172 2. Experimental details

173 A two-fluid atomizer (shown in figure 1(a)), where a central liquid jet is injected coaxially
174 along with an annular gas jet, is used here to generate the spray. The atomization process
175 is initiated when the liquid jet comes in contact with the turbulent gas. In the atomizer,
176 the central liquid jet with exit diameter d_l , resulting in the exit area $A_l = \pi d_l^2/4$, is fully
177 developed, and controlled by the volume flow rate of Q_l . Subscripts l and g represent the

Case	U_l (m/s)	Re_l	U_g (m/s)	Re_g	We_g	M	m	SR
1	0.6	1 120	82	52 000	210	23	0.24	0, 0.8
2	0.6	1 120	115	72 700	420	46	0.17	0, 0.8
3	0.6	1 120	163	102 400	830	90	0.12	0:0.2:1
4	0.6	1 120	203	127 700	1 280	140	0.1	0, 0.8
5	1.2	2 230	163	102 400	830	23	0.24	0, 0.8
6	2.3	4 350	163	102 400	830	6	0.47	0, 0.8
7	4.5	8 480	163	102 400	830	2	0.91	0, 0.8

Table 1: The table of conditions for characterizing swirling sprays, reporting the associated liquid Reynolds number $Re_l = \frac{U_l d_l}{\nu_l}$, gas Reynolds number $Re_g = \frac{U_g \sqrt{4A_g/\pi}}{\nu_g}$ and Weber number $We_g = \frac{\rho_g U_g^2 d_l}{\sigma}$, gas-to-liquid dynamic pressure ratio $M = \frac{\rho_g U_g^2}{\rho_l U_l^2}$, liquid mass loading $m = \frac{\rho_l A_l U_l}{\rho_g A_g U_g}$ and Swirl ratio $SR = \frac{Q_{SW}}{Q_{NS}}$. The axial location where measurements take place is $x/d_g = 25$ for all conditions. In addition, for case 3 with $SR = 0$ and 0.8 , the spray is investigated at $x/d_g = 10$ and 50 . At each measured axial distance, at least a dozen radial locations are probed.

178 liquid and gas phase parameters, respectively. The liquid exit velocity and Reynolds number
 179 are calculated as $U_l = Q_l/A_l$ and $Re_l = U_l d_l/\nu_l$, respectively, where ν_l is the kinematic
 180 viscosity of liquid.

181 For the gas flow, there are two sets of inlets. One set of four inlets, intended for axial
 182 gas stream at the exit, is through four streams impinging onto the atomizer axis, with a
 183 cumulative volume flow rate of Q_{NS} . On the other hand, tangential motion to the gas flow is
 184 imparted through the second set of four inlets, which are directed into the atomizer off-axis
 185 as shown in figure 1(b), with a cumulative volume flow rate of Q_{SW} . These two sets of inlets
 186 combine in the gas nozzle to provide the total volume flow rate of gas, $Q_g = Q_{NS} + Q_{SW}$.
 187 The acquired swirl in the gas flow is characterized by the swirl ratio, $SR = Q_{NS}/Q_{SW}$. The
 188 annular exit of the nozzle has inner and outer diameters as D_l and d_g , resulting in the gas exit
 189 area, $A_g = \pi(d_g^2 - D_l^2)/4$. The gas exit velocity (U_g), Reynolds number (Re_g) and Weber
 190 number (We_g) are calculated as Q_g/A_g , $U_g \sqrt{4A_g/\pi}/\nu_g$ and $\rho_g U_g^2 d_l/\sigma$, respectively, where
 191 ν_g is the kinematic viscosity, ρ_g is the density of the gas and σ is the surface tension of the
 192 liquid and gas interface. In addition to parameterizing the liquid and gas flow separately, they
 193 are combined through the gas-to-liquid dynamic pressure $M = \rho_g U_g^2/\rho_l U_l^2$ and liquid mass
 194 loading number $m = \rho_l A_l U_l/\rho_g A_g U_g$.

195 In the present experiments, distilled water is used for liquid and filtered compressed air
 196 for the gas phase. Note that all the physical properties of water and air are considered at
 197 20°C, which was the average room temperature while conducting the experiments and less
 198 than 1.5°C variation were noted around this average. The experimental facility is a recurring
 199 one as used in Tolfts *et al.* (2023, 2024) and has been characterized well in proximity to the
 200 operating range in the present study. A Proportional–integral–derivative (PID) controller is
 201 used to keep the liquid and gas flow rates constants over the measurement period. They are
 202 measured along with droplet measurements so that the actual measured average flow rate (and
 203 not set values) are used to compute non-dimensional groups. In addition, this variation over
 204 the measurement duration (up to 25 minutes) were always less than 2% over all conditions.
 205 The flow conditions for the present experiment are given in table 1.

206 The measurements of the resulting drops after atomization are performed using a phase

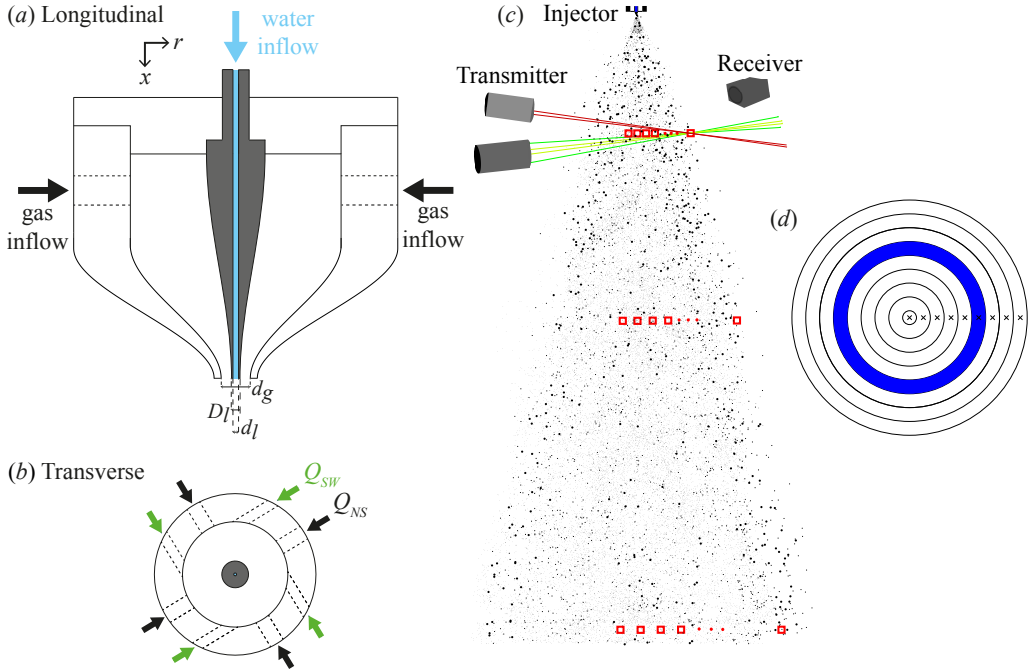


Figure 1: Spray generation configuration and measurement technique. Coaxial atomizer used in the present experiments in a longitudinal cut (a), and (b) a cross-section in the plane of the gas inlets. (c) Phase Doppler particle analyzer arrangement and measurement locations in a spray longitudinal view and (d) cross-sectional view, with annuli of area S_i representing each measurement location i .

207 Doppler particle analyzer (PDPA) as shown in figure 1(c, d). The PDPA is configured in a
 208 forward scattering mode with the scattering signal receiving angle (θ) of 49° for measuring
 209 droplet size (d), axial (u_x), radial (u_r) and tangential (u_θ) velocities in a coincident mode.
 210 The size and velocity measurements are considered point-wise and the measurement system
 211 is raster-scanned at different radial locations. The droplets were phase-validated to ensure
 212 accuracy in the measurements. The collimating lens ($f_c = 500$ mm) and the imaging lens
 213 ($f_i = 500$ mm) were used with a constant magnification ($\beta = -f_i/f_c$). The pairs of laser
 214 beams corresponding to u_x and u_r intersect to form a prolate spheroid. The probe for the
 215 third pair intended to compute u_θ is at 30° with respect to the other transmitter and intersects
 216 at the exact location (aligned to cross the probe volume with a pinhole of $50 \mu\text{m}$). The length
 217 of this probe volume is truncated using the spatial filter whose slit width is $s = 200 \mu\text{m}$.
 218 Together with the receiving probe angle and the magnification, the effective length of the
 219 cylindrical probe volume is $s/|\beta|\sin\theta$. With a motive to find the cylindrical cross-section of
 220 the probe volume, which is dependent on the size of droplets due to the Gaussian nature of
 221 the laser beam, we find the product of the axial velocity of the droplets and the residence
 222 time to find the size-dependent path length l (Albrecht *et al.* 2003). A fit to determine the
 223 relation of l with binned diameters of droplets was applied during the post-processing of the
 224 data. Using all the configuration values, we find the probe's cross-sectional area,

$$\mathcal{A} = \frac{\ell s \cos \gamma}{|\beta| \sin \theta}, \quad (2.1)$$

226 and the probe volume,

$$227 \quad \mathcal{V} = \frac{\pi \ell^2 s \cos \gamma}{4 |\beta| \sin \theta}, \quad (2.2)$$

228 where γ is the angle subtended by u_x with u_r .

229 In the present measurements, the drop size is in the range of $d = 1 - 100 \mu\text{m}$. This
 230 size range is considered to accurately characterize the surrounding gas phase in the spray,
 231 conditioning for the small droplets, and also to measure a significant proportion of the droplet
 232 population. From the small droplets, we determine the Stokes number *a posteriori* based on
 233 the exit conditions of the nozzle, given by:

$$234 \quad St_d = \frac{\tau_p}{d_g/U_g}, \quad (2.3)$$

235 where $\tau_p = \rho_\ell d^2 / (18 \rho_g \nu_g)$ is the droplet response time scale. This Stokes number (St_d) is
 236 calculated for droplets of different sizes d . We observe that for $d < 5 \mu\text{m}$, St_d for different
 237 gas Reynolds numbers under investigation is always less than 0.002. With the increase in
 238 the downstream distance of the droplets, the Stokes number also decreases quickly as the
 239 flow time scale $\propto x^2$ in a particle-laden jet flow (Hardalupas *et al.* 1989). Such droplets were
 240 therefore assumed to be the tracer particles of the gas phase.

241 Due to the choice of range that does not capture the entirety of the droplet population
 242 for a few locations and conditions, we will only discuss PDF (since although “clipped” they
 243 are not biased by that) and arithmetic mean diameter, given by $d_{nm} = \sum_i N_i d_i^n / \sum_i N_i d_i^m$ with
 244 $n = 1$ and $m = 0$, where N represents the number of drops corresponding to each drop size
 245 bin d_i . The arithmetic mean diameter in most cases here correspond to the most probable
 246 droplet size. We refrain from analyzing other diameters like d_{20} or d_{32} to avoid truncated
 247 calculations of the contribution from bigger droplets.

248 In addition, we characterize the gas phase in the absence of the spray and for non-swirling
 249 conditions using a single probe hotwire anemometer. The measurements are acquired at a
 250 sampling rate of 20 kHz for 10 seconds at each location. As a straight gas jet is known to have
 251 the radial velocity u_r one order of magnitude less than the axial velocity u_x (Pope 2001),
 252 this measurement was considered robust enough to understand the axial flow characteristics
 253 with minimal bias.

254 3. Spray formation mechanisms

255 The spray development from the near atomizer to the far-field is presented in figure 2 (Movies
 256 corresponding to these conditions are in the Supplementary Materials). The left half of each
 257 subfigure is the non-swirling condition ($SR = 0$), and the right half is the swirling condition
 258 ($SR = 0.8$). Very evident from the instantaneous snapshots is the large-scale flapping motion
 259 of the liquid jet at low M (figure 2(a)) due to which the non-swirling spray near the atomizer is
 260 seen tilted to the left side. In contrast, the swirling jet is not visible very close to the atomizer,
 261 being tilted to the opposite side in figure 2(b). Supplementary Movies reveal a high degree of
 262 flapping in the case of swirling sprays compared to their non-swirling conditions, qualitatively
 263 confirming that the increased flapping amplitude reported at low We_g by Kaczmarek *et al.*
 264 (2022) also occurs at higher gas Weber numbers. The consequent spatially varying spray
 265 structure is distinct, which appears to be less dense for $SR = 0$ than for $SR = 0.8$, the
 266 scattering signal being less pronounced indicating that the swirling cases produce a higher
 267 number of smaller droplets here. The red marks at $x/d_g = 25$ indicate the location where
 268 $u_{x,0}$ equals the mean centerline velocity of the gas jet, $u_{0,1}(x, r_{0,1}) = u_x(x, r = 0)/10$. An
 269 imaginary line (not drawn here as a measurement of the virtual origin is lacking here) joining

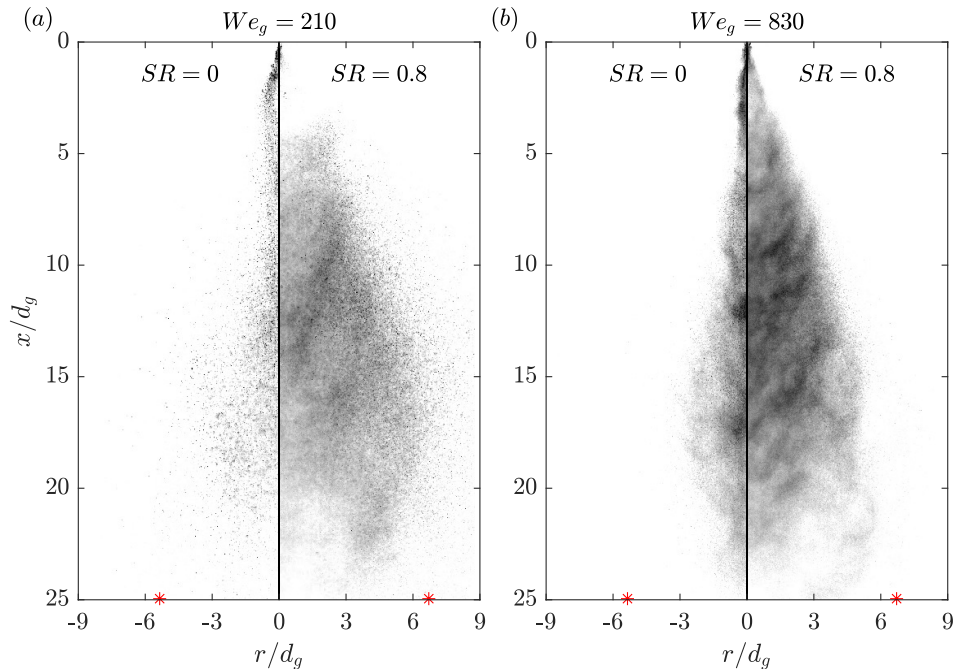


Figure 2: Spray scattering images showing the global spray features at $SR = 0$ (left half of the subfigure) and $SR = 0.8$ (right half of the subfigure) with their respective $r_{0,1}$ locations given in red marks at $x/d_g = 25$ for $Re_1 = 1120$ and (a) $We_g = 210$, (b) $We_g = 830$. The spatial inhomogeneities, especially visible in (a), are a direct signature of the flapping instability.

270 the atomizer exit and the $r_{0,1}$ location indicates an increase in the angle of the swirling gas
 271 jet compared to a non-swirling one. In addition, numerous large droplets eject beyond this
 272 limit at various axial distances at low M for both the $SR = 0$ and 0.8 . The observation for
 273 $SR = 0$ matches with the findings of Huck *et al.* (2022).

274 Different from this behavior, at high M , the spray is less affected by the flapping instability
 275 (which occurs at higher frequency, and over a smaller amplitude) near the atomizer (figure
 276 2(b)) with the presence of spatially varying intermediate and high drop density regions farther
 277 away. This may be considered as a visual indication of the larger role played by turbulent
 278 fluctuations in sprays at higher M . A keen observation of the $r_{0,1}$ locations indicates two
 279 important features at high M : (i) while for $SR = 0$ almost all the droplets are within an
 280 imaginary line joining the atomizer exit and the $r_{0,1}$ (similar observation as of Huck *et al.*
 281 (2022)), droplets go beyond this line for the swirling spray, (ii) the $r_{0,1}$ location almost
 282 remains unchanged in comparison to low M at fixed SR , indicating that the spreading is not
 283 affected much due to change in We_g if the swirl ratio is constant.

284 A few important questions that arise for better understanding the resultant spray of figure
 285 2 are how the droplet velocity varies with different parameters, what is the consequent
 286 droplet distribution, and how does spray dispersion behavior vary with governing parameters.
 287 Longmire & Eaton (1992) reported that, in the case of particle-laden jets, large-scale eddies
 288 of the gas jet contribute to the transport of particles. Moreover, in the case of swirling jets, in
 289 addition to the helical structures, three-dimensional motions are imposed. In light of this fact,
 290 although there is a higher tangential flux of the gas at higher We_g for the same swirl value,
 291 it does not lead to more spread of the droplets. Therefore, in the next section, we investigate
 292 the carrier phase to determine the counter-intuitive nature of the spread of droplets.

293 4. Kinematics

294 We remind the reader here that the measurement of the gas jet is conducted using hotwire
 295 anemometry in the absence of spray and using the small droplets in its presence. For a more
 296 detailed explanation of the methodology, the reader is referred to Section 2. From these
 297 measurements, we investigate the first-order statistics of all the velocity components of the
 298 gas to characterize the carrier phase in the presence of spray.

299 4.1. Mean axial velocity (u_x)

300 The behavior of the axial velocity of the turbulent annular gas jet is shown in figure 3.
 301 Figure 3(a) presents the radial profiles of the mean axial velocity (u_x). Lines and markers
 302 represent the hotwire and PDPA data, respectively. The symmetry of the annular gas jet in the
 303 absence and presence of spray is demonstrated here at different axial locations. Apart from
 304 the obvious decay and spread of the jet with increasing downstream distance, the significant
 305 spread of the swirling jet compared to its non-swirling counterpart is evident. In addition,
 306 the increase in the difference between the mean velocity of the gas jet in the absence and
 307 the presence of the spray can be noted as the gas jet evolves downstream. Modarress *et al.*
 308 (1984); Shuen *et al.* (1985) have previously attributed this to the presence of fully or partly
 309 responsive particles in a turbulent gas jet, whereby there is a mean slip of particles that leads
 310 to momentum transfer to the gas from the particle phase. Since $St_d > 1$ near the atomizer
 311 for many droplets, it is understood that the primary momentum transfer occurs here from the
 312 gas phase to the liquid phase, in addition to part of the gas kinetic energy being utilized by
 313 the spray formation mechanisms.

314 A summarized version of the profiles is illustrated through the jet centerline decay and
 315 spread. Figure 3(b) shows the inverse centerline axial velocity of the gas jet, $u_{x,0}(x) =$
 316 $u_x(x, r = 0)$ normalized with the exit gas velocity, U_g . In single phase gas jet measurements
 317 $u_{x,0} \propto (x - x_0^{u_x})^{-1}$ beyond the developing region ($x/d_g \geq 7$), where $x_0^{u_x}$ is the virtual origin
 318 based on the decay rate of the jet's centerline velocity. In order to quantify this evolution
 319 and also compare the changes in the presence of spray, we calculate the centerline profile as
 320 defined by Panchapakesan & Lumley (1993); Lau & Nathan (2014); Huck *et al.* (2022):

$$321 \quad \frac{U_g}{u_{x,0}} = \frac{1}{B} \frac{x - x_0^{u_x}}{d_g}, \quad (4.1)$$

322 where $1/B$ is the average decay rate and $x_0^{u_x}$ is the virtual origin associated with it. Different
 323 values of the gas jet's parameters from the literature are provided in table 2. We observe a small
 324 deviation of the single-phase gas jet (black line) from the data of Panchapakesan & Lumley
 325 (1993) (blue line). This difference may be due to the fact that while the present configuration
 326 is an annular gas jet, the experiments of Panchapakesan & Lumley (1993) consider a round
 327 jet. A higher decay rate of the annular gas jet agrees with the results of Kuhlman (1987) as
 328 shown in table 2. Moreover, measurements of gas flow from the spray droplets point to a
 329 decrease in its decay rate in the case of a non-swirling spray, indicating a modification of the
 330 carrier phase flow. The observations of Huck *et al.* (2022) regarding the decay of the gas jet,
 331 therefore, are closer to the observations of Panchapakesan & Lumley (1993); however, this is
 332 an outcome of a trail of physical phenomena. Combining the information that an annular jet
 333 yields a bigger decay rate value than a round jet (Kuhlman 1987) and that, for particle-laden
 334 coaxial jets for similar mass loading, adding particles to jet decreases its decay rate (Park &
 335 Chen 1989), our observations, with different decay rates in single or two phase conditions
 336 are in good agreement with the literature accounting all the physical traits.

337 For a swirling spray, there are significant deviations from the non-swirling case. The

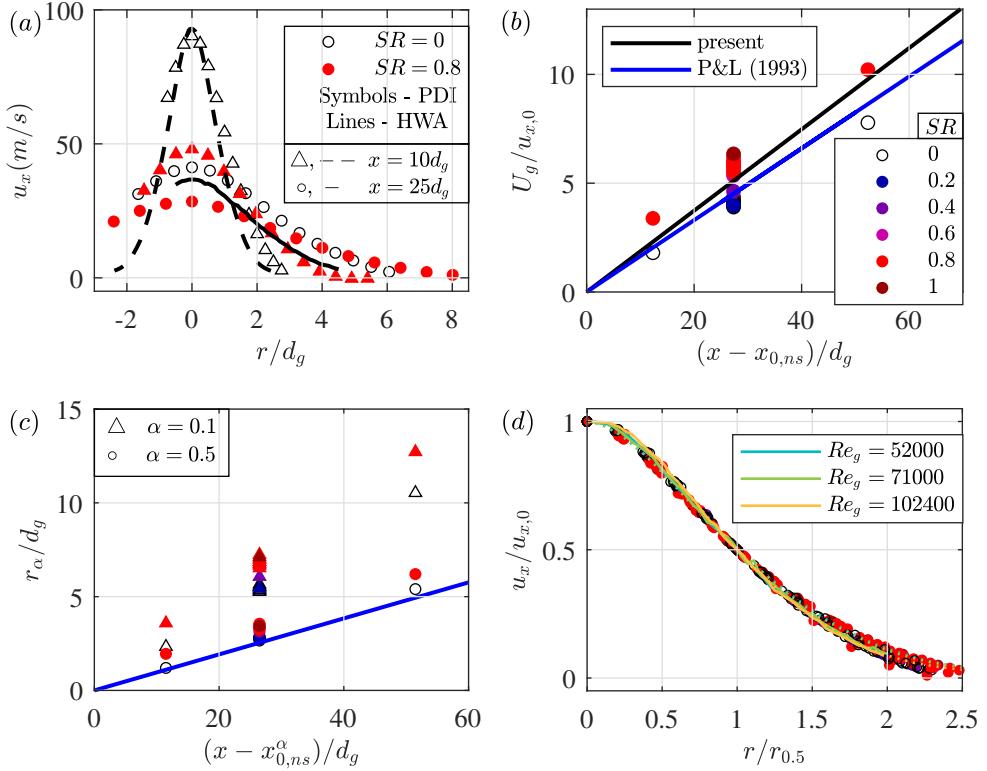


Figure 3: Gas-phase mean axial velocity (u_x) characterization in spraying (PDPA) and non-spraying conditions (hotwire anemometry, HWA). Non-swirling flow conditions are indicated by open markers from PDPA measurements (conditioned on only droplets whose size is below $5 \mu\text{m}$) and swirling conditions are shown in filled markers. (a) Comparison of the PDPA (symbols) and hotwire anemometer (lines) radial profiles of the mean axial velocity at $x/d_g = 10$ (Δ and $-$) and 25 (\circ and $-$) for $Re_g = 102400$. For PDPA, red filled symbols indicate swirled sprays. (b) Longitudinal decay of the centerline mean axial velocity along the axial distance, identifying one virtual origin ($x_{0,ns} = -2.4d_g$) for $SR = 0$ and using the same for all other conditions ($SR > 0$). The gas flow statistics obtained from all Re_l and Re_g (listed in table 1) are added with different colors depending on their SR value. The same convention is used for rest of the subfigures in this figure and figure 5. The blue line is from the round jet experiments of Panchapakesan & Lumley (1993). (c) Spreading of the annular gas jet displayed using the non-dimensional half-width (\circ) and the 10% width (Δ). $x_{0,ns}^\alpha$ represents the virtual origin corresponding to $\alpha = 0.5$ or 0.1 for $r_{0.5}$ and $r_{0.1}$. (d) Normalized mean axial velocity as a function of the non-dimensional radial coordinate $r/r_{0.5}$. The displayed conditions span all Re_g , Re_l , and SR values from table 1, as well as all the explored longitudinal locations x . The dashed and solid underlying lines represent data obtained using hotwire anemometer at both $x/d_g = 10$ and 25 .

338 possible deviations are in virtual origin, decay rate, and spreading rate. While the limitation
 339 of the data does not reveal the virtual origin ($x_{0,sw}$), it indeed points to an increase in the
 340 decay rate of velocity with an increase in SR . Such an increase is a consequence of the
 341 increased length scale associated with the swirling motion for a given axial transport of both
 342 the dispersed and continuous phases. More consequences of this behavior will be elaborated
 343 in the sections ahead.

344 The conservation of momentum of a turbulent jet necessitates a linear increase in the jet
 345 width as it evolves downstream. To represent this spread, the half width ($r_{0.5}$), which is the

Authors	B	$x_0^{u_x}$	$S_{0.5}$	$x_0^{0.5}$	$S_{0.1}$	$x_0^{0.1}$	$\theta_{0.5}^{u_x}$	$\theta_{0.1}^{u_x}$
-	-	(cm)	-	(cm)	-	(cm)	(deg)	(deg)
Panchapakesan & Lumley (1993)	6.1	0	0.096					
Huck <i>et al.</i> (2022)	6.7	-2.4	0.093	-3.8	0.182	-2.6	10.6	20.6
Kuhlman (1987) (Round jet)	6.9	-2.2						
Kuhlman (1987) (Annular jet)	4	-4						
Current (PDPA)	6.7	-2.3	0.104	-1.5	0.202	-1.6	11.8	22.8
Current (Hotwire)	5.4	0.4						

Table 2: Comparison of the jet decay and spread constants for a single-phase jet and in the presence of spray from Eq. 4.1-4.3. Note that here $d_g = 1$ cm.

346 radial location where $u_x = 0.5u_{x,0}$, is identified. This radius is related to the axial distance
 347 through:

$$348 \quad r_{0.5} = S_{0.5} \left(x - x_0^{0.5} \right), \quad (4.2)$$

349 where $S_{0.5}$ is the spreading rate at the half width and $x_0^{0.5}$ is the virtual origin corresponding
 350 to the jet half-width. In addition, with a similar definition, the ten-percent width ($r_{0.1}$) is also
 351 calculated. This radius is considered the jet edge on many occasions and is the location where
 352 entrainment plays a significant role. Figure 3(c) illustrates both radii. It is observed here that
 353 due to the increase in the decay rate with the increase of swirl in the gas jet, there is also an
 354 increase in its spreading rate. This is somewhat inferred from the $r_{0.5}$ plots and vividly from
 355 the $r_{0.1}$ plots. The jet angles, which are direct representatives of spread, are obtained from
 356 the evolution of r_α , with $\alpha = 0.5$ and 0.1 , as:

$$357 \quad \theta = 2 \tan^{-1} (S). \quad (4.3)$$

358 The different values obtained for the annular gas jet with spray are close to the reported
 359 constants of Huck *et al.* (2022). Therefore, the present results extend the investigation to
 360 swirling sprays. A quantitative assessment of this angle ($\theta_{0.1}^{u_x}$) for the swirling gas jet of $Re_g =$
 361 $102\,400$ with $SR = 0.8$ indicates an approximate increase by 25% from the corresponding
 362 non-swirling condition (from 11.59° to 14.55° half cone angle). As there is very small
 363 difference in the spread of $SR = 0.8$ and 1 , figure 3(c) confirms that the 25% increase of θ
 364 is reached gradually along increments of SR values (except for $SR = 0.2$ which resembles a
 365 non-swirling spray, in agreement with previous work). A similar behavior is also observed
 366 for $\theta_{0.5}$, however, with smaller magnitudes. While the spreading rate of swirled spray may
 367 slightly vary with the gas Reynolds number, it is first and foremost determined by the value
 368 of SR .

369 For a round gas jet, the radial and axial variation of u_x is well accommodated using a
 370 self-similarity curve often given by:

$$371 \quad \frac{u_x}{u_{x,0}} = \exp(-C\eta^2), \quad (4.4)$$

372 where $\eta = r/(x - x_0^{u_x,0})$. The self-similar variable η has a corresponding value in $r/r_{0.5}$
 373 with a scale ($S_{0.5}$) to recover the same shape. In light of this understanding, a similar nature
 374 for different conditions with respect to the $r/r_{0.5}$ coordinate is illustrated in figure 3(d). It
 375 includes non-swirling as well as swirling conditions for different axial locations. There is an
 376 appreciable collapse across all the cases of table 1. This collapse is indicative of the axial

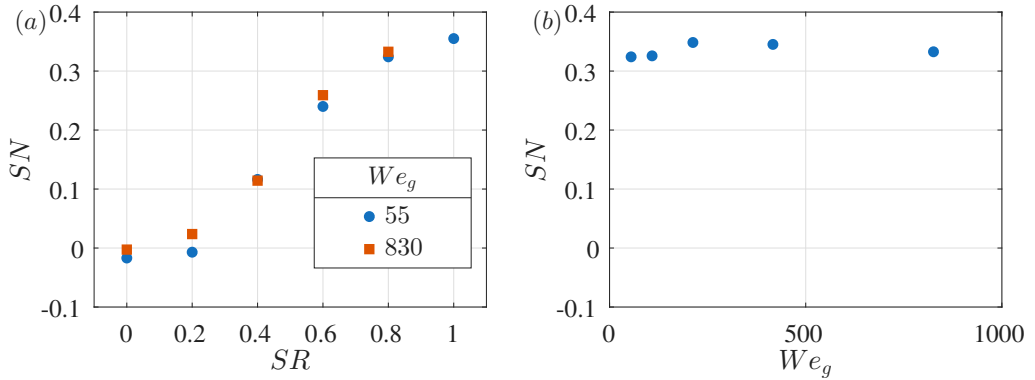


Figure 4: The swirl number SN calculated using Equation 4.5 and plotted with the swirl ratio SR for two We_g values (a) and along We_g at $SR = 0.8$ (b).

377 momentum-conserving nature of the jet, even in the presence of a swirl. However, critical
 378 information for a swirling spray also underlies other velocity components of the carrier
 379 phase, pertinent to determining the drop size and liquid mass distributions in a particular
 380 spray plane.

381 4.2. Mean radial (u_r) and tangential (u_θ) velocity of the jet

382 It is important to discuss here that the swirl ratio SR is a proxy parameter for quantifying the
 383 swirl. As the values of u_θ and u_x are not a constant value over the annular gap of the nozzle,
 384 an integrated approach is used to better characterize the swirl intensity by calculating the
 385 swirl number (SN), given by:

$$386 \quad SN = \frac{\int_0^{r_{max}} 2\pi\rho u_x u_\theta r^2 dr}{r_{max} \int_0^{r_{max}} 2\pi\rho u_x^2 r dr}. \quad (4.5)$$

387 SN represents the ratio of the axial flux of the angular momentum to the axial flux of the axial
 388 momentum. This definition follows the one by Beér & Chigier (1972) and has been mentioned
 389 to be applicable for the characterization of swirl generated through different mechanisms,
 390 such as vanes, helical structures, and also by inlet-based methods (like in the present studies).
 391 The appropriateness of this parameter can be clearly observed in figure 4, which plots SN
 392 at the nozzle exit with respect to SR . The measurements are conducted 1 mm away from the
 393 atomizer using PDPA with olive oil-based smoke with sizes of the order of $1 \mu\text{m}$. Figure
 394 4(a) showcases the fact that irrespective of gas Weber number, SR characterizes the flow as
 395 well as SN , and therefore, can be used interchangeably for parameterization. The broad span
 396 of We_g values reported here encompasses the range of the spray operations of this article.
 397 Figure 4(b) shows the relation between SN and We_g for $SR = 0.8$. It further reinforces the
 398 independence of SN/SR with the change in We_g . In what follows, SR is used throughout,
 399 being the controlled parameter, as it conveys the same level of information about the swirl
 400 intensity as SN .

401 Figure 5 demonstrates the mean radial (u_r) and tangential (u_θ) velocity components of the
 402 gas jet in the presence of spray, which are roughly one order of magnitude less than u_x .
 403 The self-similar behavior of the radial velocity profile and its radial increase followed by
 404 gradual decrease is given by Pope (2001), calculated from the data of Hussein *et al.* (1994)
 405 using the continuity equation. A similar profile is also observed here for the non-swirling
 406 gas jet (figure 5(a)), although with a difference in scale as the continuity equation used by
 407 Pope (2001) will not provide exact values due to entrainment effects. In addition, we also

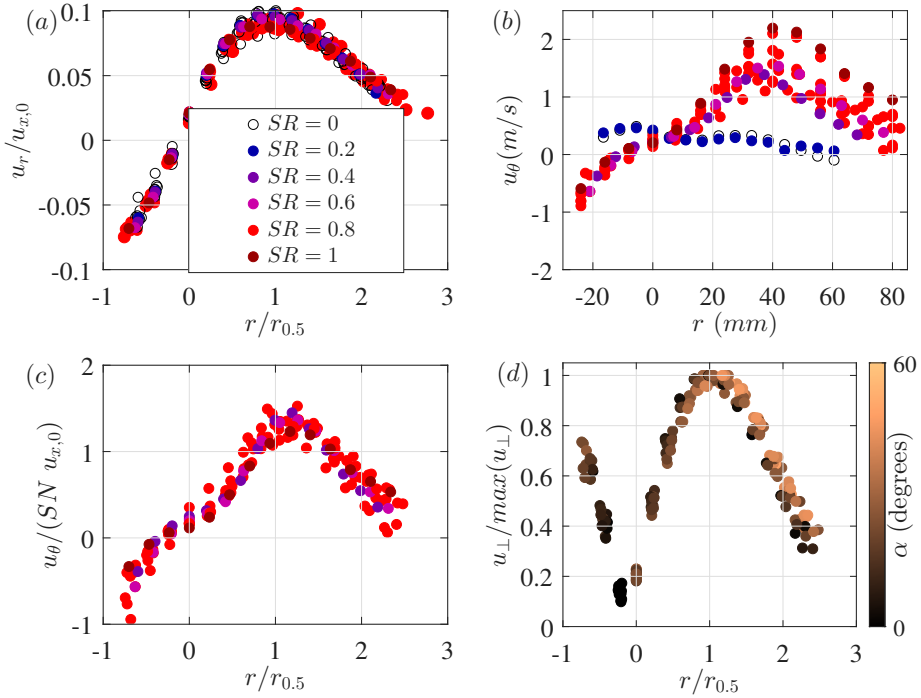


Figure 5: Gas-phase radial velocity (u_r) and tangential velocity (u_θ) characterization. All the non-swirling conditions are shown with black open circles, and swirling conditions are shown with filled circles of different colors depending on SR . (a) Radial velocity profiles normalized with their centerline axial velocity shown as a function of the radial coordinate non-dimensionalized with their half-widths of the axial velocity profiles for all the conditions in table 1. (b) Radial profiles of the tangential velocity for all cases in table 1. (c) The tangential velocity normalized with centerline axial velocity and SN (from Eq. 4.5) as a function of non-dimensional radial coordinate for $SR \geq 0.4$ at $x/d_g = 25$ for all Re_l and Re_g . (d) Non-dimensional radial profiles of the normalized velocity in the $r - \theta$ plane for $SR > 0$ in table 1 for all Re_l and Re_g at $x/d_g = [25, 50]$. The color map indicates the angle subtended by the u_\perp with the u_r .

408 observe the same profile shape for the radial velocity, even in the presence of some tangential
 409 motion in the gas flow. The measurements were restricted to the radial locations where there
 410 were enough droplets available for statistical convergence (for acquisition times limited to
 411 25 min). Nonetheless, the radial extrapolation of radial velocity profiles leads to a region of
 412 negative value, marking the entrainment region. This behavior is observed not only for the
 413 non-swirling gas jet but also for the swirling jet.

414 In a swirling flow field, along with u_x and u_r , u_θ also significantly contributes to the droplet
 415 distribution due to its contribution towards the centrifugal force. Figure 5(b), therefore,
 416 demonstrates the radial behavior of the tangential velocity, which establishes the fact that
 417 the spray encounters a meaningful tangential velocity only when $SR \geq 0.4$. Hence, the
 418 comparisons of the characteristics of the swirling spray with the non-swirling spray are
 419 primarily conducted with $SR = 0.8$. The mean tangential velocities for conditions with
 420 $SR \geq 0.4$ at a particular axial location can be non-dimensionalized with a product of
 421 the axial location's centerline velocity and swirl number (SN) given by Eq. 4.5. This non-
 422 dimensional tangential velocity is plotted along the radial distance normalized by $r_{0.5}$. Figure
 423 5(c) presents this profile, which is self-similar across different SR and flow conditions but
 424 not across axial locations. The definition of SN establishes that the relative angular velocity

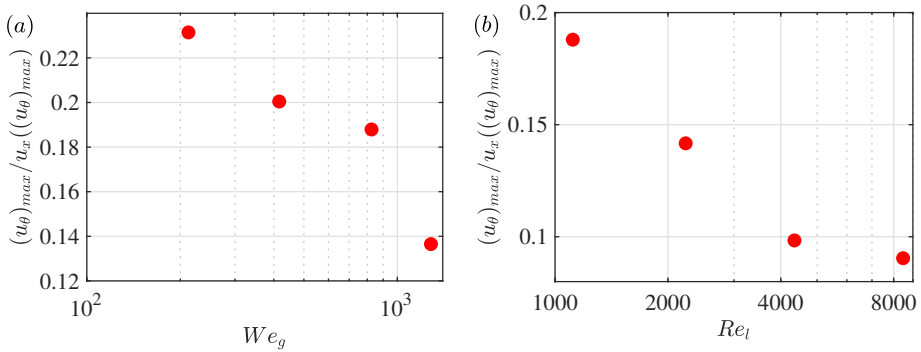


Figure 6: Swirl value of the gas phase calculated from the data for $SR = 0.8$ and $Re_g = 102400$ at $x/d_g = 25$.

425 of the gas jet at different radial locations concerning the centerline axial velocity is nearly a
 426 constant factor defined by the ratio of axial flux of angular momentum and axial flux of axial
 427 momentum.

428 Although most of the momentum is in the axial direction, with a minor contribution from
 429 u_r and u_θ , together they can affect migration of the droplets which may result in a change in
 430 the dispersion behavior of droplets. To cater the lateral flowfield in a combined manner, the
 431 velocity in the perpendicular plane of the spray axis, given by $u_\perp = \sqrt{u_r^2 + u_\theta^2}$ are normalized
 432 by their maximum value and plotted with the radius non-dimensionalized with $r_{0.5}$ in figure
 433 5(d). The profile is similar to non-dimensional u_r and u_θ profiles. In addition, the angles
 434 subtended by u_\perp with u_r are high only for $r > r_{0.5}$. However, the converse may not always
 435 be true, as observed from the plot. It is observed that r_{crit} , the radial location where u_\perp is
 436 maximal, roughly coincides with $r_{0.5}$. The self-similarity of u_\perp and u_x establishes a conserved
 437 nature of the spray, independent of swirling intensity, whereby appropriate identification of
 438 the similarity parameters can result in the unique description of the spray, irrespective of
 439 condition and location.

440 Until now, the mean velocity profiles have mostly been normalized with centerline axial
 441 velocity. However, a better essence of the swirling motion comes from its normalization with
 442 the axial velocity for that location, which is shown in figure 6 along We_g and Re_l . It indicates
 443 that, for a constant SR value, the swirling intensity of the gas decreases with increasing We_g
 444 as a higher swirling velocity at the exit of the nozzle is associated with high shear and a more
 445 considerable effective distance covered by the fluid particle, resulting in higher dissipation
 446 with respect to the axial motion. On the other hand, with an increase in Re_l , more kinetic
 447 energy is required for breakup and dispersion, which leads to a smaller contribution to the
 448 tangential velocity. It is important to note here that the mechanism of loss of the swirling
 449 motion with increasing We_g and Re_l are different. Consequently, the droplet dispersion at
 450 higher We_g and Re_l are affected differently, which will be elaborated in further sections.

451

4.3. Droplet slip

452 The gas phase on interaction with the droplets determines the latter's dispersion. A classical
 453 way of representation has been to investigate the slip of the big droplets in the surrounding
 454 gas phase. While particles with $St < 0.01$ are typically considered to behave as tracer
 455 particles (Balachandar & Eaton 2010), for a more optimistic determination of the gas phase,
 456 we consider $St < 0.002$ as a limit for identifying particles as tracers of the gas jet. On the
 457 other hand, the bigger particles with Stokes number, $St > 0.01$, are known to accumulate at
 458 regions of high strain rate (Eaton & Fessler 1994). As a result, particles in a high-speed jet

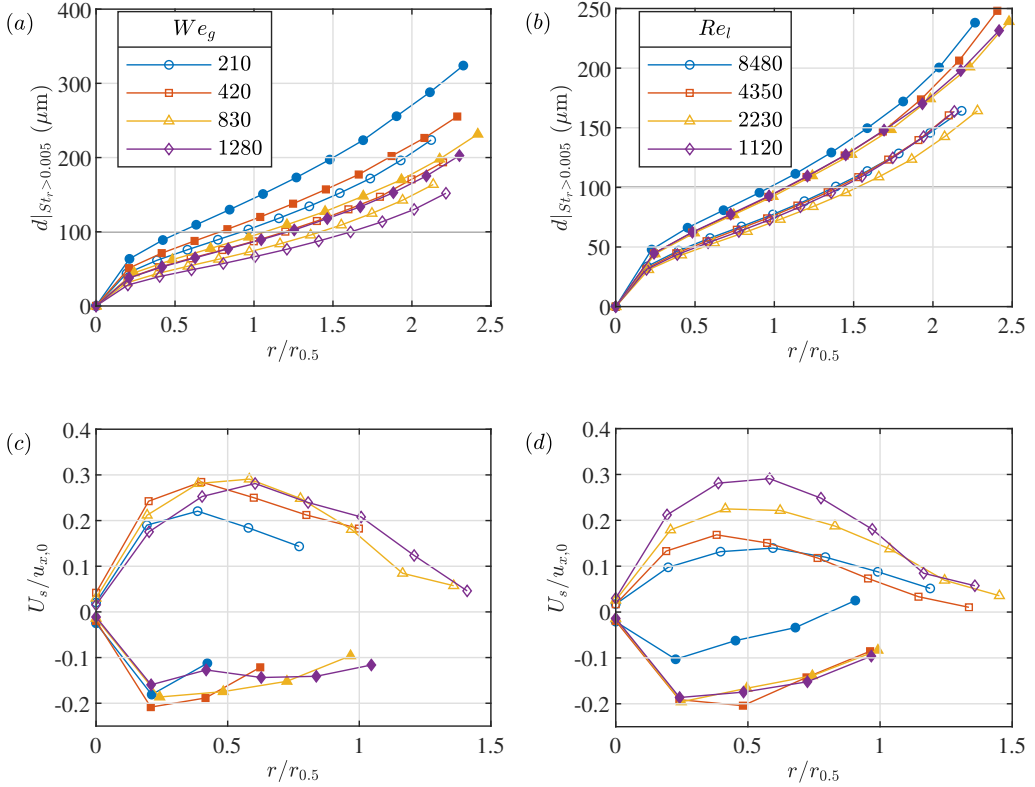


Figure 7: Radial profiles for the computed average size of drops whose local Stokes number respects $St_r > 0.005$ with varying (a) We_g and (b) Re_l for swirling (open markers) and non-swirling (filled markers) conditions. The horizontal $100 \mu\text{m}$ line indicates the limit of droplet size measurement in this study. Radial profiles of slip velocity defined by the velocity difference of droplets with $St_r > 0.005$ and $u_{g,x}(r)$ for different (c) We_g and (d) Re_l .

459 exhibit some slip relative to the carrier flow. In a polydispersed spray, the size of droplets
 460 varies widely, resulting in $St_d \sim 10^{-4}$ at the nozzle exit for the present investigation, where
 461 the subscript d indicates droplet here. Considering that the droplets for which $St_d > 0.005$
 462 are either partially responsive or non-responsive, we investigate the slip behavior of these
 463 droplets in figure 7. To find this slip velocity (U_s), we first compute the size class of droplets
 464 that yields $St_r > 5 \times 10^{-3}$, defining a local Stokes number where the flow timescale is based
 465 on the radius of the location (r) as length scale divided by the mean local gas axial velocity.
 466 This formulation leads to a radial increase in the average drop size used in the definition as
 467 the location is farther from the jet center which is shown in figure 7(a, b). Therefore, U_s is
 468 limited to the radial location for which $d_{|St_r>0.005} < 100 \mu\text{m}$, since this corresponds to the
 469 biggest drop measured. Then, we find the average axial velocity of these droplets for which
 470 $d_{|St_r>0.005} < d < 100 \mu\text{m}$ and calculate the difference from the gas mean axial velocity
 471 $U_s(r) = \langle v_{x|St_r>0.005} \rangle(r) - u_x(r)$. Note that from here, plots with open and filled markers
 472 will represent $SR = 0$ and $SR > 0$, respectively.

473 Compared to the gas flow, the big droplets in a non-swirling spray accelerate, overshoot the
 474 gas flow, and then decelerate as they transport downstream (Lasheras *et al.* 1998; Zhou *et al.*
 475 2022; Wu *et al.* 2022). At $x/d_g = 25$, $U_s > 0$ at the centerline, as noticed in figure 7(c, d),
 476 which is either in the overshoot or deceleration region. This is in confirmation of the results

477 on particle-laden jets (Hardalupas *et al.* 1992) and sprays (Lasheras *et al.* 1998). The slip
 478 velocity, U_s , increases with radius from the centerline and decreases after reaching a maxima.
 479 The radial profiles observed here are similar to the trends observed by Wu *et al.* (2022) in
 480 sprays and can be interpreted from the results of Zhou *et al.* (2022) on particle-laden jets. The
 481 reason for an off-center maximum is the higher particle inertia of the large droplets, which
 482 leads to high velocity far downstream while the gas jet spreads more rapidly, thereby decaying
 483 faster (Gounder *et al.* 2012). Eventually, when $r/r_{0.5} > 1$, the Stokes number experienced
 484 by the big droplets becomes small enough to attain a velocity value close to that of the gas
 485 phase. These results are also complemented by the fact that U_s decreases with higher Re_l
 486 closer to the centerline (figure 7(c)) and is indicative of the late response of the big droplets,
 487 which occurs at farther downstream distance from the exit of the atomizer. Therefore, the
 488 inertia attained is also low.

489 With swirl added to the gas jet, the increase in spreading leads to a reduced mean axial
 490 velocity of the carrier flow, however, much smaller than the one found for the droplet
 491 velocities. As a result, figure 7(c, d) demonstrates that $U_s < 0$ for most radial locations
 492 accessible here, reaching a minimum before increasing again with the radius. In addition, no
 493 specific correlation was observed with We_g or Re_l . Considering droplets that are centrifuged
 494 away from the jet's centerline, carrying high axial momentum accumulated there and carried
 495 over to regions of $r > 0$, one may expect droplet velocities larger than that of the carrier flow.
 496 On the contrary, droplets that are formed by high-amplitude flapping events, commonly found
 497 in swirled sprays, are ejected directly outside of the gas jet and may find their way back to the
 498 jet only due to entrainment, explaining their low axial velocities. Combining these statements
 499 the averaged droplet velocity is found largely to be smaller than in non-swirling conditions,
 500 indicating that there may be a larger proportion of initially detrained droplets that are then
 501 entrained back into the jet than droplets centrifuged from the jet's axis. An exception is the
 502 $Re_l = 8480$ condition displaying a lower negative amplitude of U_s . In comparison to the
 503 other conditions, the high momentum liquid jet may in that case produce more large droplets
 504 in the vicinity of the centerline whose high inertia better preserves their axial momentum as
 505 they get centrifuged radially, leading to positive slip velocity close to $r = r_{0.5}$.

506 5. Droplet size distribution

507 An essential component of characterizing any spray is deciphering the drop size variation
 508 with different governing parameters. To address this, we focus on a point-wise and a global
 509 statistical description of the spray. These assessments will help to take a step towards
 510 characterizing the spatial description of the liquid mass distribution. We want to point
 511 out that the present measurements are restricted to a drop size up to $100 \mu\text{m}$.

512 5.1. Local drop size characteristics

513 A noteworthy feature of coaxial sprays is the production of drops with a wide range of sizes,
 514 which one can assess from the droplet distribution plots shown in figure 8. While the peaks of
 515 the distributions are found below $10 \mu\text{m}$, the mean droplet size can vary with radial location
 516 by typically tens of μm , depending on the condition (not shown here). The 70 to $100 \mu\text{m}$
 517 range is found to approximately plateau for most conditions and locations as shown in figure
 518 8.

519 The spray formation mechanism explained for high We_g (Marmottant & Villermaux 2004;
 520 Huck *et al.* 2022) lead to larger mean droplet size in the center of the spray than at the edge
 521 in the absence of swirl. We show the probability distribution functions of drop sizes for
 522 such a condition for a fiber-type atomization regime at different radial locations for a non-
 523 swirling spray in figure 8(a), which confirms the established understanding. An addition of

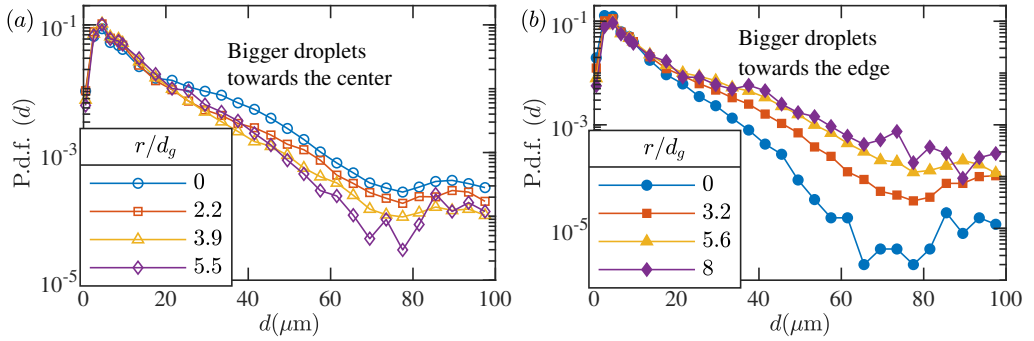


Figure 8: Probability density functions at several radial locations for a given longitudinal distance $x/d_g = 25$, for $Re_l = 1120$ and $We_g = 830$ at (a) $SR = 0$ and (b) $SR = 0.8$

524 swirl (shown in figure 8(b)) can be observed to reverse the spatial sampling of droplets in
 525 the spray, with smaller droplets found at the center. This change indicates the manipulative
 526 influence of the centrifugal force in rearranging droplets in a spray plane, based on their
 527 mass ($F_c = m_d \omega^2 r$, m_d is the mass of droplets and $\omega = u_\theta / r$), and hence, size. Such
 528 behavior contributes to an increase in the spray angle beyond the gas jet angle for a swirling
 529 spray as the large droplets are flung far due to F_c (Préaux *et al.* 1998). This explanation
 530 is complemented by the smaller eddy turnover time near the toroidal region close to the
 531 atomizer for high swirling flows, due to which only the small droplets that have a small
 532 response time are entrained. This argument also holds good for conditions with low We_g .
 533 However, as the mechanism of droplet breakup and entrainment in low We_g conditions favor
 534 the same organization of droplets with and without swirl, no change is noticeable with such a
 535 representation and will require a different description, which we provide later in the following
 536 subsection.

537 On the other hand, for low We_g conditions, the origin of droplets of different size ranges
 538 varies, and hence, their dynamics differs in the carrier phase. Chigier & Farago (1992)
 539 have reported that liquid jet breakup with low We_g , and hence low Re_g , is a regime where
 540 atomization predominantly occurs through the formation and bursting of bags, contributing
 541 to form much finer droplets than expected at these We_g values (if bags were absent). Its rims
 542 and ligaments form large droplets, following similar processes as for the breakup of a single
 543 droplet subjected to a gas flow. In addition, due to the flapping behavior of the liquid jet at
 544 these low We_g , the outward ejections of large droplets result in a droplet distribution peak
 545 $\sim 100 \mu\text{m}$ at the spray edge. Calculating the Weber number of these big droplets based on
 546 slip velocity, the value obtained is less than 1, indicating no further breakup of these drops
 547 is possible. It is well-known that the spread of a gas jet results in mass entrainment. While
 548 droplets with $St < 0.01$ can certainly respond to entrainment and attain an inward radial
 549 velocity, the droplets with $St > 10$ have a ballistic motion. This behavior is distinguishable
 550 primarily near the atomizer, where the breakup occurs. Combining the above understandings
 551 points to the fact that only finer droplets can get influenced by entrainment ($\propto u_x$) and have
 552 a higher probability of accumulating near the center of the spray. Therefore, the droplet
 553 distribution favors small droplets at the center and large ones at the edge (not shown) for low
 554 We_g . This understanding confirms the results obtained by Huck *et al.* (2022).

555 Figure 9(a) and (b) shows the radial profiles of the mean drop size at different axial
 556 locations for high We_g non-swirling and swirling conditions, respectively. These measure-
 557 ments reveal two aspects of spray development as droplets travel downstream in a turbulent
 558 environment. In the case of non-swirling and swirling sprays, we observe that at high We_g for

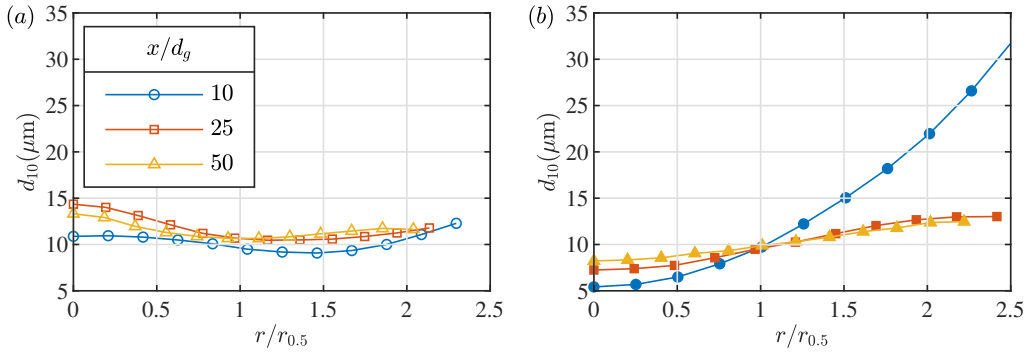


Figure 9: The mean droplet size (d_{10}) plotted with radius non-dimensionalized with $r_{0.5}$ for $Re_l = 1120$ and $We_g = 830$ at various axial distances x/d_g . (a) $SR = 0$, and (b) $SR = 0.8$.

559 $x/d_g = 25$ and 50, the drop size profiles are almost identical, indicating the fully-developed
 560 nature of the spray. Comparing these profiles to the profiles at $x/d_g = 10$, two completely
 561 different behaviors can be observed for non-swirling and swirling conditions. For the non-
 562 swirling condition, one can observe a slight increase in the drop size throughout the spray
 563 with almost the same shape as observed at $x/d_g = 25$ and 50. This indicates a very minor
 564 rearrangement due to entrainment, but mostly coalescence of the droplets throughout the
 565 spray. On the other hand, for a swirling spray, the profile changes drastically, crossing the
 566 other two profiles at $r = r_{0.5}$, with drop size as the spray's edges more than double the
 567 values found further downstream. The profiles change from the centrifugal sorting near the
 568 atomizer to homogenization due to turbulence far from the nozzle. Therefore, we conduct
 569 further investigations on the radial profiles of the drop size at $x/d_g = 25$, by which time the
 570 radial profiles have evolved to a fully-developed profile for all conditions.

571 Figure 10 demonstrates the influence of different parameters on the radial variation of the
 572 mean drop size for a non-swirling and a swirling spray. A logical way forward is first to
 573 understand the influence of various swirl intensities and then downsize the investigation to a
 574 few conditions. Therefore, figure 10(a) highlights the changing nature of the mean droplet
 575 size radial profiles with increased swirl intensity. Such a radial variation of the drop size
 576 (albeit for the Sauter mean diameter d_{32}) is also observed by Pr aux *et al.* (1998) and (for
 577 d_{10}) by Fong *et al.* (2024). The invariance of the profile for $SR < 0.4$ is in confirmation to the
 578 inference obtained from figure 5(c) that there is a limited effect of swirl in such cases. The
 579 radial d_{10} profile changes from a “~” shape at negligible swirl values to a “U” shape when
 580 the swirl effects exist. To quantify this change we describe a two-location identifier of the
 581 shape d_{10} at $r/r_{0.5} = 1 : 2$ (normalized by the value at $r = 0$) given by [a b]. Measuring the
 582 shape identifier for the conditions in figure 10(a), we find that this value changes from [0.74
 583 0.8] for $SR = 0$ to [1.24 1.61] for $SR = 1$. When the radial profile shape is “~”, as in the
 584 former condition, the shape identifier value decreases slightly (from 1 to 0.74 here) and then
 585 increases (from 0.74 to 8 here). For a “U” profile, as in the later condition, the value increases
 586 monotonously with a larger relative amplitudes (1, 1.24, and 1.61 here). For $SR \geq 0.4$, one
 587 can observe in addition a decrease in the drop size with increasing swirl throughout the radial
 588 extent of measurements. This behavior can be attributed to the increased probability of the
 589 small droplets closer to the center and an indication of a decrease in the overall size of the
 590 droplets with increasing swirl for high We_g . These results are in agreement of the findings
 591 of Fong *et al.* (2024).

592 Figure 10(b) and (c) compares the effect of swirl on drop size for different We_g without

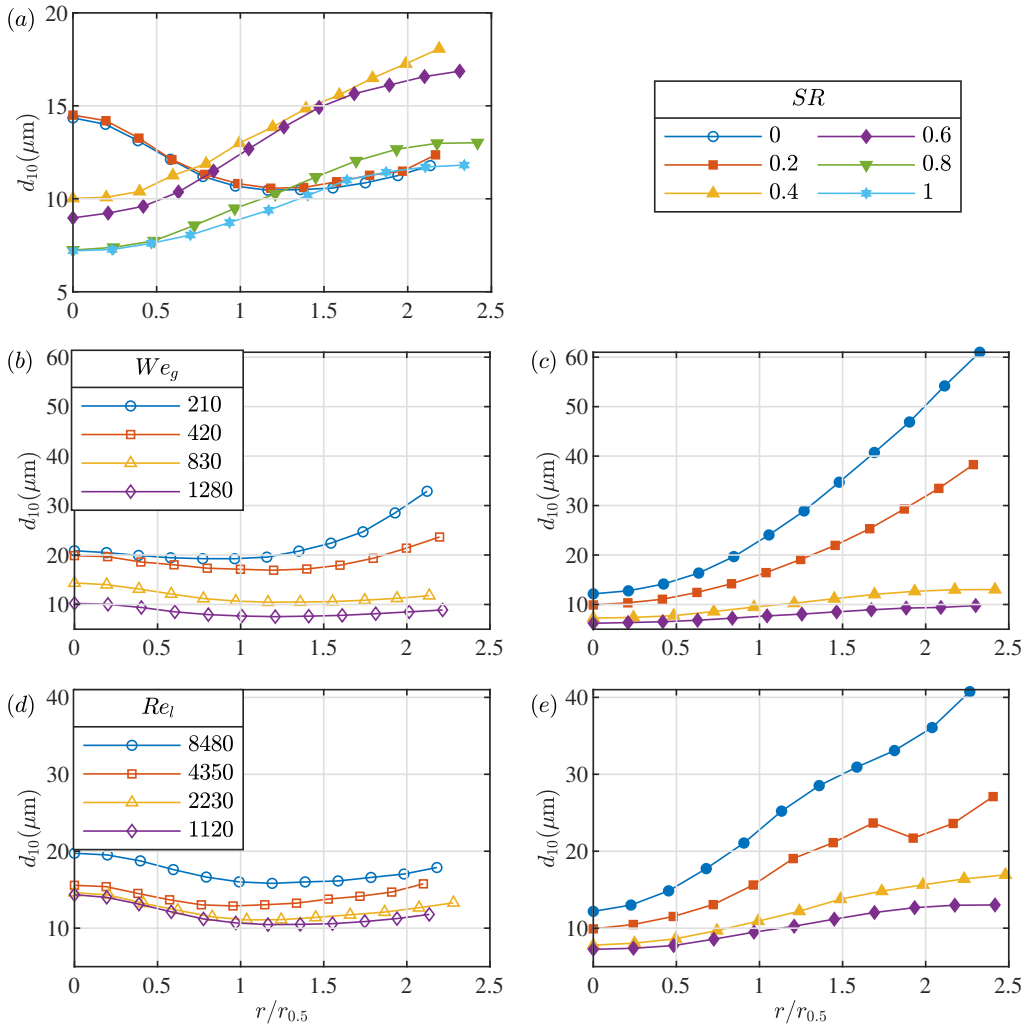


Figure 10: The mean droplet size (d_{10}) plotted with radius non-dimensionalized with $r_{0.5}$ for different flow conditions at $x/d_g = 25$. (a) $We_g = 830$, $Re_l = 1120$ for different SR values. (b, c) Fixed $Re_l = 1120$ at different We_g values and (d, e) Fixed $We_g = 830$ at different Re_l values. (b, d) $SR = 0$, and (c, e) $SR = 0.8$

593 and with swirl. The drop size decreases throughout a particular spray plane with an increase
 594 in We_g , irrespective of the swirl. However, a closer look at the radial drop size profiles for
 595 non-swirling sprays (figure 10(b)) suggests that the shape identifier value changes from [0.92
 596 1.4] for $We_g = 210$, indicating almost a “U” shape with very high values at the edge, to [0.75
 597 0.83] for $We_g = 1280$, indicating a “~” shape. For swirling conditions (figure 10(c)), this
 598 profile retains the “U” shape for all We_g due to the explanation given above. Nonetheless,
 599 the curvature of the profile, i.e., the steepness of the radial increase in mean droplet size,
 600 can be observed to decrease with the increase in We_g for the later conditions. The change
 601 is especially striking for the two higher We_g values, such that the drop sizes do not deviate
 602 significantly in all the spatial domains and are in the closer range found for non-swirling
 603 sprays. The shape identifier value varies from [1.88 4.14] for $We_g = 210$ to [1.22 1.51] for
 604 $We_g = 1280$, indicating the drastic change in the magnitudes of the radial variations making

605 the spray much more homogeneous in terms of droplet size (going from a fourfold to a 50%
 606 increase only). These results lead to the inference that three factors contribute to defining the
 607 shape of the droplet size radial profiles: (i) the higher gas kinetic energy with increasing We_g
 608 leading to the formation of smaller droplets, which are influenced by entrainment, (ii) the
 609 increase in the unfavorable pressure gradient with increase in u_θ , and (iii) the independence
 610 of S_c from M at high M (Hopfinger & Lasheras 1996). Altogether, these factors reduce
 611 the preferential segregation of droplets for higher We_g . Nevertheless, a subtle difference
 612 in the radial profile from the “U” shape is the change from a monotonic increase without
 613 noticeable inflection point ($\frac{d^2d}{dr^2} \geq 0$) at low We_g to the presence of profiles with inflection
 614 point ($\frac{d^2d}{dr^2} = 0$) at higher We_g , either side of which the curvature changes sign.

615 While a similar investigation for two values of We_g on radial drop size profiles has been
 616 demonstrated recently by Fong *et al.* (2024), an investigation into the effect of Re_l on a
 617 non-swirling spray is elaborated here. Figure 10(d) shows that although there is a change in
 618 the magnitude of radial drop size profiles with increase in Re_l , there is barely any change in
 619 its shape, contrary to the effect of We_g . For the non-swirling spray, the “~” radial drop size
 620 profile varies from the shape identifier value of [0.81 0.87] at $Re_l = 8480$ to [0.74 1.1] at
 621 $Re_l = 1120$. This examination substantiates the significant role that We_g plays in the initial
 622 liquid jet breakup mechanisms over Re_l (Lasheras & Hopfinger 2000; Tolfts *et al.* 2023),
 623 leading to the drop size profiles. On swirl addition to the gas flow (figure 10(e)), the radial
 624 profiles are “U” shaped. Specifically, this shape has a similar inflection for conditions with
 625 small Re_l and large We_g values. The associated shape factors are [1.87 2.92] for $Re_l = 8480$
 626 and [1.32 1.76] for $Re_l = 1120$, indicating a significant change in the size between the
 627 edge and the center. Focusing on both parameters indicates that the gas-to-liquid dynamic
 628 pressure ratio M may have a role in determining the drop size profiles for swirling sprays.
 629 However, our efforts in combining the effect of Re_l and We_g through M does not provide
 630 any direct correlation. This behavior confirms that the relationship between drop size and the
 631 flow parameters is non-trivial. With more results, this aspect is elucidated further in Section
 632 7.

633 5.2. Global drop size characteristics

634 Most of the literature has focused on a radial change of drop size, which is a point-wise
 635 measurement with a variable contribution to the global spray based on the radial location.
 636 Elaboration of this representation is shown through figure 1(d), where each cross represents
 637 the radial location and the annular space represents the area that each of these locations
 638 (blue annulus for one of the locations is highlighted as an example) is assigned to. Therefore,
 639 in order to make the contributions of each radial location a justifiable proportion of the
 640 global spray, we define a probability distribution function as follows (Tratnig & Brenn 2010;
 641 Dhivyaraja *et al.* 2019; Osuna Orozco 2021; Fong *et al.* 2024):

$$642 \quad p_i = \frac{\sum_j N_{ij} S_j / w_i T_j}{\sum_i \sum_j N_{ij} S_j / w_i T_j}, \quad (5.1)$$

643 where N_{ij} is the number of particles in droplet size class i at location j , S_j is the area
 644 which the location j represents (Figure 1(d)), w_i is the weight of the droplet size class i
 645 depending on the diameter of the probe volume, which is required for rectifying the bias due
 646 to the Gaussian nature of the laser beam and T_j is the time of collection of data at location
 647 j . The weighting function w_i is determined by fitting a logarithmic curve fitting between the
 648 drop size and the path length of the droplets in the probe volume. The cumulative probability
 649 distribution function is plotted for different We_g and Re_l in figure 11(a) and (b) respectively

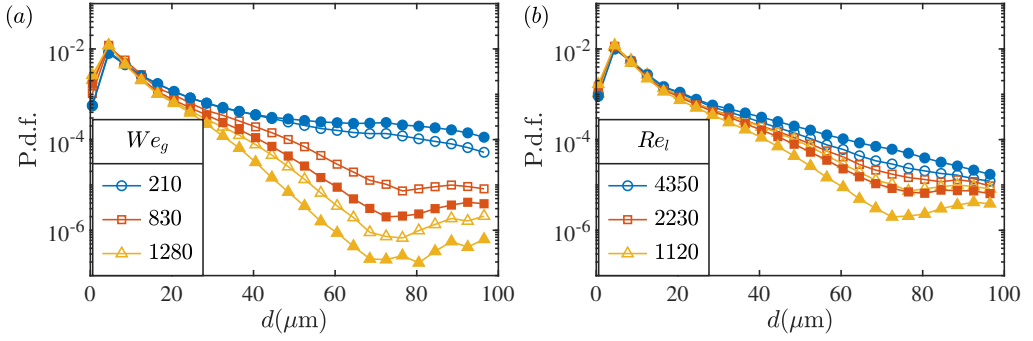


Figure 11: Global drop size distributions for different We_g for $Re_l = 1120$ (a) and $Re_l = 830$ (b), at $x = 25d_g$. Empty symbols correspond to non-swirling conditions while filled ones are for $SR = 0.8$.

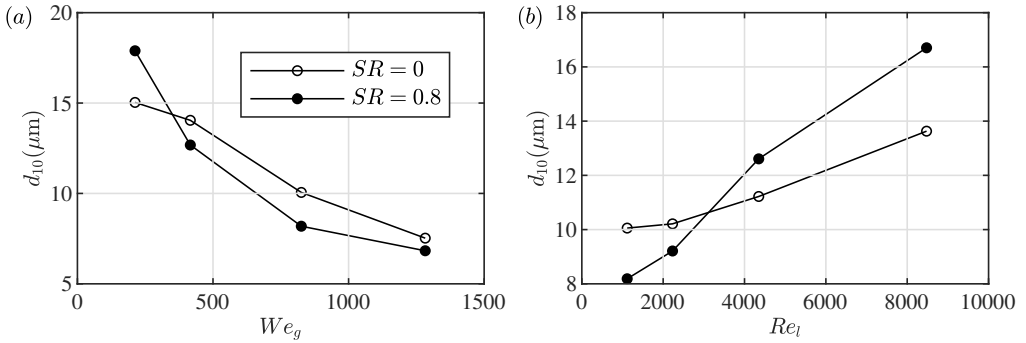


Figure 12: Variation of the global mean drop size d_{10} with We_g for $Re_l = 1120$ (a) and Re_l for $We_g = 830$ (b), at $x = 25d_g$. Empty symbols correspond to non-swirling conditions while filled ones are for $SR = 0.8$.

650 for non-swirling and swirling sprays. One can notice that at low We_g and high Re_l , there is
 651 a higher probability of bigger droplets for the swirling spray compared to the non-swirling
 652 one, and the converse is true for high We_g and low Re_l . However, when swirl assists the
 653 spray (e.g., at high We_g and low Re_l) the reduction in the probability of large droplets is
 654 massive, with for instance a probability decrease of a factor roughly 3-5 in the 50 to 80 μm
 655 range. The resulting drop size (d_{10}) from Eq. 5.1 is shown in figure 12. One can observe a
 656 decrease of drop size with the increase in We_g and the converse with increasing Re_l due to
 657 the increased inertia compared to the surface tension forces with increasing M . While the
 658 spread of the spray due to swirl is well known, this analysis gives a global assessment of
 659 the drop size. We conclude that swirl reduces the drop size for high M . However, it may
 660 have a detrimental effect in terms of drop size at lower M . The recently presented results on
 661 the mean drop size by Fong *et al.* (2024) claims that there is a monotonous decrease in the
 662 size for the whole spray droplet size with the introduction of swirl for $M = 25$ and 56, and
 663 hence, for all regimes of spray. However, the present exploration to further lower M and also
 664 different Re_l values indicates a complicated relation between the global drop size depending
 665 on Re_l , We_g and SR . In this way, the present result extends the existent findings on findings
 666 of Fong *et al.* (2024) on the effects of gas swirl on drop size.

667 6. Dispersion

668 Although the carrier phase and the drop size descriptions provide a significant understanding
 669 of the spray, these assessments are incomplete without realizing how the liquid mass flow
 670 rate gets distributed in a spray plane. Therefore, in this section, we comprehensively assess
 671 the influence of the characterized carrier phase and deciphered drop size variations on the
 672 spatial liquid volume distribution. This quantity is best explained through dispersion, which
 673 includes characterizing the fluxes, and its relative response in the carrier phase gas flow.
 674 This section will help us relate different observations of the swirling spray to the existing
 675 understanding of non-swirling sprays.

676 6.1. Axial flux

677 The preceding discussion on gas phase velocity and drop size have elucidated two important
 678 features of the swirling spray: (i) High axial gas velocity at the center of the spray (figure 3),
 679 and (ii) Large droplets at the edge of the spray (figure 10). Individually, they do not apprise
 680 whether the mass flux will be high at the center due to high velocity or at the edge due to
 681 the large droplet size, which is essential to assess liquid mass distributions. Therefore, we
 682 calculate the volume flux of the liquid at a particular location by

$$683 \quad \dot{g}_x = \frac{\pi}{6T} \sum_{i=1}^D \sum_{j=1}^{N_i} \frac{d_{j,i}^3 \cos(\theta_j)}{\mathcal{A}_i}, \quad (6.1)$$

684 where T is the collection time (at the measurement location), $d_{j,i}$ is the size of the j th drop
 685 in the i th bin and $\theta_j = \tan^{-1}(u_r/u_x)$. \mathcal{A}_i is the size-dependent probe area given in Eq. 2.1.
 686 Figure 13 illustrates the influence of different flow parameters on the radial profiles of axial
 687 volume fluxes (\dot{g}_x), non-dimensionalized by their centerline values. For a non-swirling flow,
 688 the narrowing of the volume flux profiles with increasing We_g has been reported earlier by
 689 Hardalupas & Whitelaw (1994); Huck *et al.* (2022), which is also observed here. In addition,
 690 we observe opposite trends with an increase in Re_l , confirming the role of M in determining
 691 the axial flux profiles.

692 On the other hand, although the volume flux profiles for the swirling flows follow a similar
 693 relationship with We_g and Re_l , they deviate from the bell-shaped radial profile. Especially
 694 for low M values, the radial decrease is non-monotonic, and the maxima shifts away from
 695 the centerline which is similar to the observations made by Fong *et al.* (2024) for the swirling
 696 conditions they investigated. In addition to these observations, the present investigation
 697 also highlights that depending on the liquid Reynolds number, in corresponding high We_g
 698 conditions, the centerline can also have the maximum flux at a radial distance away from
 699 the spray axis. Note that our assessment does not associate a definitive M for this transition
 700 across varying Re_l , leading to a non-trivial relation of the change of shape of the radial flux
 701 profiles with M for swirling sprays.

702 The liquid jet breakup near the atomizer involves its orbiting about the axis of the atomizer
 703 when swirl is introduced (Machicoane *et al.* 2020; Kaczmarek *et al.* 2022). In the presence
 704 of this swirling gas, a large portion of the big droplets, and hence mass, are expected to
 705 centrifuge outside. However, the influence is predominant when the initial droplet formation
 706 happens sufficiently away from the axis, so adequate angular momentum is available. At low
 707 M conditions, the orbiting liquid jet has a long length and will have a substantial propensity
 708 to break farther away from the axis and attain higher angular momentum, thereby shifting
 709 the maximum flux away from the centerline (found in the vicinity of $0.5 < r/r_{0.5} < 1$).
 710 Extrapolating this understanding to high M conditions, due to very short breakup length
 711 in the case of high M conditions, such a possibility is difficult due to the pre-existing high

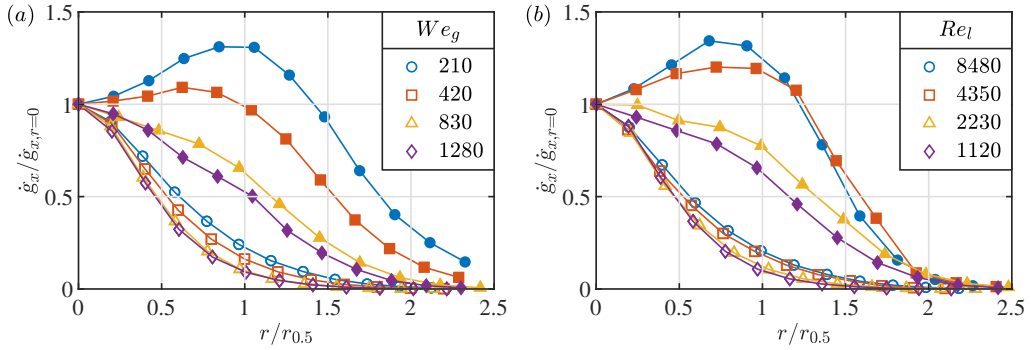


Figure 13: Radial profiles of axial flux with (a) $Re_l = 1120$, (b) $We_g = 830$ measured at $x = 25d_g$. Open and filled symbols represent the non-swirling and $SR = 0.8$ conditions, respectively.

712 confinement effects close to the atomizer ($\propto U_g$). Nevertheless, the spread of the gas jet
 713 further downstream and the corresponding transport of droplets facilitate the liquid mass to
 714 deviate away from the centerline due to the swirling motion of the gas, resulting in a broader
 715 bell curve, whose maximum is still located at $r = 0$. Whether swirled high M conditions
 716 bear axial flux whose radial profiles can retain the shape of their non-swirling counterpart is
 717 unclear and would require more data, but the radial spread increases when swirl is impeded
 718 to the gas jet. This explanation can be complemented with the observations of Fong *et al.*
 719 (2024). Their results indicate that at a given gas-to-liquid momentum ratio M (with 25 and
 720 56 sampled in their study), roughly similar shapes of radial volume flux profiles are observed
 721 through the gradual increase of swirl when its effect is noteworthy, with a clear broadening of
 722 the profiles. On closer inspection, high-swirl conditions present profiles that remain constant
 723 over a small subset of radial values (up to $2d_g$), before they decrease. We also observe
 724 similar results for low M in the same range of the parametric values as they examined. For
 725 higher M conditions, adding swirl to the gas jet makes the profile wider but approximately
 726 retains the non-swirl shape across different $SR > 0.2$ values explored here. The combined
 727 understanding, therefore, is that the shape of the radial profile of axial fluxes are determined
 728 by the value of M even in the presence of swirl. Depending on the value of M , swirl may
 729 then change the shape of the profiles.

730

6.2. Droplet response at the edge

731 The spray edge is often considered an identifier of the spray formation method (Acharya *et al.*
 732 2021; Huck *et al.* 2022). In addition, the response of specific-sized particles to particular
 733 eddies has been demonstrated, e.g. for shear layer by Lazaro & Lasheras (1992) and for gas
 734 jet by Chung & Troutt (1988); Longmire & Eaton (1992); Sbrizzai *et al.* (2004). The Eulerian
 735 time scale for these eddies is based on the large-scale helical structures existing in a gas jet
 736 and given by

$$737 \quad T_E = 2r_{0.1}/u', \quad (6.2)$$

738 where u' is the centerline turbulent axial velocity fluctuation. The length scale $2r_{0.1}$ associated
 739 with this time scale for the jet is due to the correlation of the eddies with its width (Tso &
 740 Hussain 1989; Yoda *et al.* 1992), which we analyze at $r_{0.1} < r < r_{0.05}$ as its validity has been
 741 demonstrated throughout the jet cross-section by Prevost *et al.* (1996). The mean droplet size
 742 at this radial location is used to calculate the time scale by

$$743 \quad \tau_p = \rho_l \langle d_p \rangle^2 / (18\nu_g \rho_g). \quad (6.3)$$

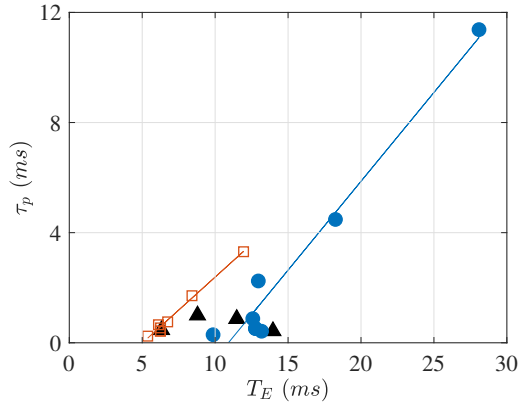


Figure 14: Droplet time scale based on mean size compared with the Eulerian time scale at the spray edge. \square , \triangle and \circ represent $SR = 0$, > 0 and $= 0.8$ conditions respectively

744 This relation is plotted in figure 14. The corresponding Stokes number is given by

$$745 \quad St = \tau_p / T_E, \quad (6.4)$$

746 which is ~ 0.1 or greater for all cases. These values indicate that the large eddies at the
 747 edge of the spray, which are evidenced both in non-swirling and swirling gas jets, will affect
 748 at least partially the droplets' trajectories, e.g. with the occurrence of radial ejections of
 749 the inertial droplets and loitering. In swirling conditions, these eddies are accompanied
 750 by helical structures that may play an additional role in spray dispersion. For non-swirling
 751 sprays (red squares), the relation between large eddy time scale and mean droplet time scale
 752 is linear with varying conditions. This observation indicates that as the mean droplet time
 753 scale increases due to an increase in its size, so does the eddy size to which such drops can
 754 respond. The analysis of Huck *et al.* (2022) considers the peak droplet size in the distribution
 755 at the edge for varying axial locations for a single condition in a spray and the resulting Stokes
 756 number ~ 1 to claim the role of the helical eddies in transporting the big droplets by ejection.
 757 Their analysis was restricted for $M \lesssim 50$ when the ejections occurred. In contrast, the
 758 present analysis spans all We_g and Re_l values given in table 1. The present result underlines
 759 a universality of the droplet behavior at the edge, irrespective of the regime.

760 Extending such an analysis to swirling sprays, we observe that with a gradual increase in
 761 SR , the timescale of eddies increases that responds to even bigger droplets at the edge (as
 762 observed in figure 10) as traced from figure 14: The red squares representing $SR = 0$ are
 763 followed by black triangles going from left to the right of the plot representing $SR = 0.2$ to
 764 0.6 until the blue circles. Subsequently, the circles are indicative of $SR = 0.8$, and again,
 765 a triangle to its right is for $SR = 1$. The droplet versus the eddy time scale plot for $SR = 0.8$
 766 (blue circles) is also observed to be almost linear like their non-swirling counterpart, although
 767 with a higher dispersion. Note that the helical structures in the case of swirling spray also have
 768 a contribution from the tangential component of velocity. The consequence is an increase
 769 in the time scale of axial fluctuations due to the eddies at the edge, which is larger than the
 770 droplet response time scale due to bigger drops.

771 7. Discussion and conclusion

772 After its role in the initial breakup of the liquid jet, the gas jet also bears significance in the
 773 droplet redistribution. At gas Weber numbers of 210 and 420, for the swirling conditions, the
 774 far-field swirl number value shown in figure 6 is greater than 0.2, indicating high swirling

Re_g	We_g	M	SR	d_{10}	d_{20}	d_{32}	d_{43}
102400	830	90	0	10.06	14.33	35.11	49.81
102400	830	90	0.8	8.18	11.59	28.46	42.1
127700	1280	140	0	7.53	10.47	24.8	36.92
127700	1280	140	0.8	6.83	9.26	20	28.49

Table 3: Different characteristic diameters $d_{nm} = \left[\frac{\sum p_i d_i^n}{\sum p_i d_i^m} \right]^{\frac{1}{n-m}}$ (in μm), where p_i is the probability of each drop size class d_i for $Re_l = 1120$ measured at $x = 25d_g$ for two gas velocities without and with gas swirl.

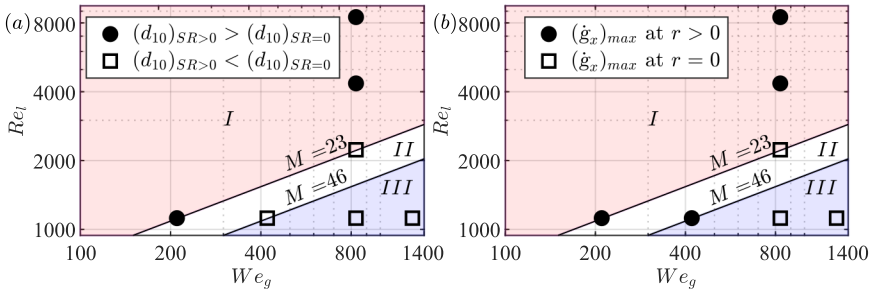


Figure 15: Regime map for separating swirling sprays based on (a) global drop size if swirl assists or hinders atomization and (b) the radial profile of axial flux displays a maximum at the spray's center or away from it.

775 intensity at $r \approx r_{0.5}$. On the other hand, the drop size profile shown in figure 10(b) for
 776 the non-swirling condition has a “U”-shaped profile. Combining together these two observations,
 777 swirl addition in the gas jet leads to high intensity azimuthal velocities that makes the radial
 778 drop size profile “U”-shaped without any inflection point. For all other conditions in figure
 779 6(a-b), the far-field swirl value is less than 0.2, and as mentioned above, we observe that the
 780 shape of the radial profile of d_{10} remains solely driven by We_g , as the gas jet longitudinal
 781 momentum and its associated entrainment are the determining factors for such cases.

782 In addition to drop size radial profiles, the moments of the drop size for the whole spray
 783 can be assessed, yielding different characteristic diameters to quantify the influence of swirl
 784 (Table 3). Considering the range of diameter that can be measured in the present configuration,
 785 this is limited to $We_g \geq 830$, to ensure that the entirety of the droplet size distributions are
 786 captured to prevent biases in estimating higher order moments. Assessing the role of We_g
 787 from the first and third rows, we infer that not only d_{10} but also d_{32} and d_{43} decreases by
 788 roughly 25% when the gas Weber number increases by 55%. Such a synchronous change
 789 across different characteristic diameters indicates that the P.d.f. is roughly shifted as a whole
 790 towards smaller sizes. On the other hand, comparing rows 3 and 4, on gas swirl addition,
 791 while d_{10} decreases by roughly 10%, d_{32} and d_{43} decreases by approximately 25%, indicating
 792 that in addition to an overall droplet size reduction, the big drops are particularly affected by
 793 swirl and broken into smaller ones for this high Weber condition. At a slightly smaller gas
 794 Weber number (rows 1-2), swirl addition more or less shift the droplet size distribution to
 795 smaller sizes, with a reduction of the drop size moments of roughly 20% .

796 The global P.d.f. shown in figure 11 can be categorized into two kinds. One is a P.d.f. with
 797 one mode, and the other is a P.d.f. with two modes. Such bimodal behavior usually highlights

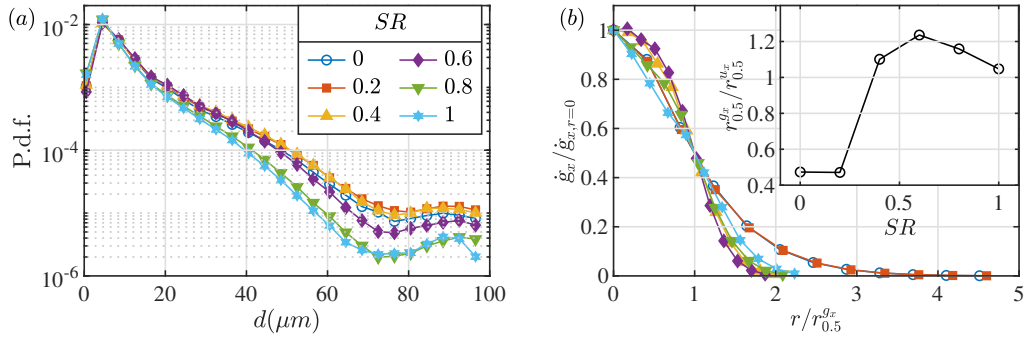


Figure 16: Global drop size distributions (a), and radial profiles of the axial flux (b) for different SR at $Re_l = 1120$ and $We_g = 830$ at $x = 25d_g$.

798 the presence of two predominant mechanisms and is associated with high M conditions
 799 here. Note that the axial flux corresponding to these conditions presents a maximum away
 800 from the center. Therefore, the segregation of small droplets towards the center due to
 801 high entrainment and centrifuging of the large droplets due to the high tangential velocity
 802 component towards the outer edge are believed to be the two mechanisms for such behavior.
 803 Based on these understandings, two regime plots are shown in figure 15. Figure 15(a)
 804 separates the conditions that are assisted by swirl in making finer droplets from the conditions
 805 where swirl hinders spray formation and figure 15(b) separates conditions when the axial
 806 flux is maximum away from the centerline from the conditions when axial flux is maximum
 807 at the centerline. It is apparent that M solely cannot define these boundaries appropriately.
 808 To sum up the observations of figure 15:

- 809 • $M < 23$ (region I) - In this region, swirl in the gas flow is responsible for producing
 810 bigger global drop size than the non-swirling condition. The axial flux in this region is
 811 strongly affected by swirl, leading to an off-center maxima in the radial profile.
- 812 • $M > 46$ (region III) - In this region, swirl in the gas flow leads to reduction in the
 813 global drop size compared to the non-swirling conditions. The radial profiles of axial flux do
 814 not change shape on swirl addition.
- 815 • $23 \leq M \leq 46$ (region II) - In this region of intermediate M , the effect of swirl is less
 816 straightforward. Low values of the liquid Reynolds number yield off-center maxima for the
 817 radial profiles of the axial flux, but can result in larger or smaller drop size depending on the
 818 Weber number. Off-centered maxima of flux profiles can be determined by $We_g < 400$ and
 819 larger drop size by $We_g < 200$ (note that these thresholds do not hold out of region II).

820 Although the above discussion for a single swirling intensity ($SR = 0.8$) distinguishes the
 821 change in two prominent features of the spray, i.e., drop size and flux, compared to the non-
 822 swirling conditions, it stays short from apprising on the dependence of these features on the
 823 swirl intensity. Therefore, gradual variations in SR values were attained for the $We_g = 830$,
 824 $Re_l = 1120$ case, found in region III of figure 15, to demonstrate these aspects and is
 825 presented in figure 16. The global drop size distributions shown in figure 16(a) are observed
 826 to have a similar bimodal distribution for all the swirling conditions as observed for figure
 827 11(a). This result reaffirms the above discussions on the influence of M in the determination
 828 of the shape of these distributions. In addition, the gradual decrease in the number of big
 829 drops with increasing swirl intensity when $SR > 0.4$ is apparent (probability densities in
 830 the $50 < d < 100 \mu m$ range are decreased by 39% and 75% at SR 0.6 and 0.8-1 compared
 831 to $SR \leq 0.4$). This effect leads to a generalized drop size reduction from the non-swirling
 832 condition. However, for $SR \leq 0.4$, the size is marginally bigger.

833 Figure 16(b) follows this up with a similar analysis of the radial profiles of axial flux for

834 varying swirling intensities, presenting radial profiles of a common shape (centered maxima
 835 of the profiles with wider bell curve), that roughly collapse when normalized by the half-width
 836 radius $r_{0.5}^{sx}$ (swirled cases display a slightly steeper shape than conditions with $SR \leq 0.2$).
 837 In addition, a drastic increase of $r_{0.5}^{sx}$ (more than doubled when $SR \geq 0.4$, see inset) as the
 838 swirl effect becomes dominant is also observed, which is in line with the explanations given
 839 with a single swirling condition (figure 13). Clearly, when the effect of swirl is tangible, the
 840 flux profiles become wider than the velocity profiles (as $r_{0.5}^{sx} > r_{0.5}$), displaying a similar
 841 shape. At the same time, the broadening of the flux radial profiles is estimated to be almost
 842 double for low M conditions, with an off-centered maximum, emphasizing the importance
 843 of the regime maps to relate liquid mass distributions in the spray. Note that Fong *et al.*
 844 (2024) also found that the radial profiles of axial flux change with SR but are not as much
 845 as the large changes reported here at low M , as they report profiles that are more or less
 846 flat in the vicinity of the centerline, then decay for larger radial distances (with a possible
 847 low-amplitude off-centered maximum). This complements the conclusions made in figures
 848 13 and 16, with a possible continuum of shapes for the radial profiles of axial flux in swirled
 849 spray as M increases. This analysis also leads to a profound understanding that swirl intensity
 850 alone, without any consideration for M values, imparts limited insight into the radial profile
 851 of droplet size and spatial variation of the mass flux. This also calls for further investigations
 852 on how the change of shape gradually occurs through variations of M for swirled spray and
 853 at varied swirl intensities. Therefore, this discussion adds immensely to the scarcely explored
 854 literature on swirling sprays.

855 In the present investigation, the characteristics of swirling sprays are compared to their
 856 non-swirling counterparts. We observed that the carrier phase velocity field is affected due to
 857 the introduction of swirl: (a) The decay rate of the axial velocity increases and consequently
 858 the spread of the jet also increases. (b) The radial velocity profile in the plane perpendicular to
 859 the axial plane is self-similar, with profiles collapsing when the radius is non-dimensionalized
 860 with $r_{0.5}$ and the velocity by its maxima. Interestingly, the axial slip of swirling sprays was
 861 observed to be negative, unlike the non-swirling sprays. The breakup mechanism is known
 862 to transition primarily due to the change in the gas Weber number We_g , so does the radial
 863 drop size profile. For the low We_g conditions in non-swirling spray, i.e., when the flapping
 864 motion of the liquid jet plays a key role in breakup, the mean droplet size d_{10} radial profiles
 865 are “U”-shaped. However, at high We_g , irrespective of the liquid Reynolds number Re_l ,
 866 the non-swirling spray is “~”-shaped, maximum at the center, then only slightly decreasing
 867 then increasing again. However, for the swirling spray, this shape is observed to be “U”-
 868 shaped, irrespective of We_g and Re_l , with the presence of inflection point. The curvature is
 869 especially high when the pressure ratio values are low. In such conditions, the maxima of the
 870 radial flux profile shifts away from the center. However, low M swirling conditions display
 871 a wider bell curve than the non-swirling spray. Based on this understanding, a regime map
 872 was established, showing the distinction between such cases, which clearly demonstrates
 873 the non-trivial nature of the dependence of spray dispersion on M values. In addition, the
 874 role of gas swirl in the assistance and hindrance of forming fine sprays at high and low M
 875 values, respectively, is represented through another regime map. Irrespective of the regimes
 876 identified for swirling conditions based on both the above mentioned criteria, and also for the
 877 non-swirling conditions, a common observation is the positive radial gradient of drop size at
 878 the edge of spray. Therefore, an investigation to identify the characteristics of the droplets at
 879 the spray’s edge for individual swirl value revealed that their linear response to the Eulerian
 880 time scales of the flow are observed to vary when the strength of the gas swirl increases.
 881 This investigation bears significance due to the increased requirement of swirling spray in
 882 different applications such as metal powder manufacturing.

883 **Funding.** This research was funded, in whole or in part, by the Agence Nationale de la Recherche under grant
 884 number ANR-22-CE30-0003-01. A [CC-BY 4.0](#) public copyright license has been applied by the authors to
 885 the present document and will be applied to all subsequent versions up to the Author Accepted Manuscript
 886 arising from this submission, in accordance with the grant's open access conditions.

887 **Declaration of Interests.** The authors report no conflict of interest.

888 **Author ORCIDs.** S. K. Sahoo, <https://orcid.org/0000-0002-6074-8825>; Y. Wei, <https://orcid.org/0000-0001-7817-9977>; N. Machicoane, <https://orcid.org/0000-0001-6492-8412>

REFERENCES

- 890 ACHARYA, AKSHAY S, DEEVI, SRIVALLABHA, DHIVYARAJA, K, TANGIRALA, ARUN K & PANCHAGNULA,
 891 MAHESH V 2021 Spatio-temporal microstructure of sprays: data science-based analysis and
 892 modelling. *Journal of Fluid Mechanics* **912**, A19.
- 893 ADE, SOMESHWAR SANJAY, KIRAR, PAVAN KUMAR, CHANDRALA, LAKSHMANA DORA & SAHU,
 894 KIRTI CHANDRA 2023 Droplet size distribution in a swirl airstream using in-line holography
 895 technique. *Journal of Fluid Mechanics* **954**, A39.
- 896 ALBRECHT, H-E, BORYS, M, DAMASCHKE, N, TROPEA, C, ALBRECHT, H-E, BORYS, M, DAMASCHKE, N &
 897 TROPEA, C 2003 *Laser Doppler and Phase Doppler Measurement Techniques*. Springer.
- 898 ANGRIMAN, SOFÍA, FERRAN, AMÉLIE, ZAPATA, FLORENCIA, COBELLI, PABLO J, OBLIGADO, MARTIN &
 899 MININNI, PABLO D 2022 Clustering in laboratory and numerical turbulent swirling flows. *Journal of*
 900 *Fluid Mechanics* **948**, A30.
- 901 BALACHANDAR, S & EATON, JOHN K 2010 Turbulent dispersed multiphase flow. *Annual review of fluid*
 902 *mechanics* **42** (1), 111–133.
- 903 BEÉR, JÁNOS MIKLÓS & CHIGIER, NORMAN A 1972 *Combustion aerodynamics*.
- 904 BILLANT, PAUL, CHOMAZ, JEAN-MARC & HUERRE, PATRICK 1998 Experimental study of vortex breakdown
 905 in swirling jets. *Journal of Fluid Mechanics* **376**, 183–219.
- 906 BRANDT, LUCA & COLETTI, FILIPPO 2022 Particle-laden turbulence: progress and perspectives. *Annual*
 907 *Review of Fluid Mechanics* **54** (1), 159–189.
- 908 CHIGIER, NORMAN & FARAGO, ZOLTAN 1992 Morphological classification of disintegration of round liquid
 909 jets in a coaxial air stream. *Atomization and sprays* **2** (2).
- 910 CHUNG, JN & TROUTT, TR 1988 Simulation of particle dispersion in an axisymmetric jet. *Journal of Fluid*
 911 *Mechanics* **186**, 199–222.
- 912 CROW, S CJ & CHAMPAGNE, FH 1971 Orderly structure in jet turbulence. *Journal of fluid mechanics* **48** (3),
 913 547–591.
- 914 DELON, ANTOINE, CARTELLIER, ALAIN & MATAS, JEAN-PHILIPPE 2018 Flapping instability of a liquid jet.
 915 *Physical Review Fluids* **3** (4), 043901.
- 916 DHIVYARAJA, K, GADDES, D, FREEMAN, E, TADIGADAPA, S & PANCHAGNULA, MV 2019 Dynamical similarity
 917 and universality of drop size and velocity spectra in sprays. *Journal of Fluid Mechanics* **860**, 510–543.
- 918 DIMOTAKIS, PAUL E, MIAKE-LYE, RICHARD C & PAPANTONIOU, DIMITRIS A 1983 Structure and dynamics of
 919 round turbulent jets. *Physics of Fluids* **26** (11), 3185–3192.
- 920 DUMOUCHEL, CHRISTOPHE 2008 On the experimental investigation on primary atomization of liquid streams.
 921 *Experiments in fluids* **45**, 371–422.
- 922 DUNAND, ARNAUD, CARREAU, JEAN-LOUIS & ROGER, FRANCIS 2005 Liquid jet breakup and atomization by
 923 annular swirling gas jet. *Atomization and sprays* **15** (2).
- 924 EATON, JOHN K & FESSLER, JR 1134 1994 Preferential concentration of particles by turbulence. *International*
 925 *Journal of Multiphase Flow* **20**, 169–209.
- 926 FAVRE-MARINET, M, CAMANO, EB & SARBOCH, JAROSLAV 1999 Near-field of coaxial jets with large density
 927 differences. *Experiments in Fluids* **26** (1), 97–106.
- 928 FONG, KEE ONN, XUE, XINZHI, OSUNA-OROZCO, RODRIGO & ALISEDA, ALBERTO 2024 Gas–liquid coaxial
 929 atomization with swirl in high-pressure environments. *International Journal of Multiphase Flow*
 930 **174**, 104767.
- 931 GOUNDER, JAMES DAKSHINA, KOURMATZIS, AGISILAOS & MASRI, ASSAAD RACHID 2012 Turbulent piloted
 932 dilute spray flames: Flow fields and droplet dynamics. *Combustion and flame* **159** (11), 3372–3397.
- 933 GÜRZING, STEFANIE, THIEBES, ANJA L, CORNELISSEN, CHRISTIAN G, JOCKENHOEVEL, STEFAN & REDDEMANN,
 934 MANUEL A 2022 Suitability of bronchoscopic spraying for fluid deposition in lower airway regions:

- 935 Fluorescence analysis on a transparent in vitro airway model. *Journal of Aerosol Medicine and*
936 *Pulmonary Drug Delivery* **35** (5), 269–277.
- 937 HARDALUPAS, Y, TAYLOR, AMKP & WHITELAW, JAMES HUNTER 1989 Velocity and particle-flux
938 characteristics of turbulent particle-laden jets. *Proceedings of the Royal Society of London. A.*
939 *Mathematical and Physical Sciences* **426** (1870), 31–78.
- 940 HARDALUPAS, Y, TAYLOR, AMKP & WHITELAW, JAMES HUNTER 1990 Velocity and size characteristics of
941 liquid-fuelled flames stabilized by a swirl burner. *Proceedings of the Royal Society of London. A.*
942 *Mathematical and Physical Sciences* **428** (1874), 129–155.
- 943 HARDALUPAS, Y, TAYLOR, AMKP & WHITELAW, JAMES HUNTER 1992 Particle dispersion in a vertical
944 round sudden-expansion flow. *Philosophical Transactions of the Royal Society of London. Series A:*
945 *Physical and Engineering Sciences* **341** (1662), 411–442.
- 946 HARDALUPAS, Y & WHITELAW, JAMES H 1994 Characteristics of sprays produced by coaxial airblast
947 atomizers. *Journal of Propulsion and Power* **10** (4), 453–460.
- 948 HOFFMANN, S, LENZE, B & EICKHOFF, H 1997 *Results of experiments and models for predicting stability*
949 *limits of turbulent swirling flames*, , vol. 78699. American Society of Mechanical Engineers.
- 950 HOPFINGER, EJ & LASHERAS, JC 1996 Explosive breakup of a liquid jet by a swirling coaxial gas jet. *Physics*
951 *of Fluids* **8** (7), 1696–1698.
- 952 HUCK, PD, OSUNA-OROZCO, R, MACHICOANE, NATHANAËL & ALISEDA, A 2022 Spray dispersion regimes
953 following atomization in a turbulent co-axial gas jet. *Journal of Fluid Mechanics* **932**, A36.
- 954 HUSSEIN, HUSSEIN J, CAPP, STEVEN P & GEORGE, WILLIAM K 1994 Velocity measurements in a high-
955 reynolds-number, momentum-conserving, axisymmetric, turbulent jet. *Journal of Fluid Mechanics*
956 **258**, 31–75.
- 957 JEROME, J, MARTY, SYLVAIN, MATAS, JEAN-PHILIPPE, ZALESKI, STÉPHANE & HOEPFFNER, JÉRÔME 2013
958 Vortices catapult droplets in atomization. *Physics of Fluids* **25** (11).
- 959 KACZMAREK, MAXIME, OSUNA-OROZCO, RODRIGO, HUCK, PETER DEARBORN, ALISEDA, ALBERTO &
960 MACHICOANE, NATHANAËL 2022 Spatial characterization of the flapping instability of a laminar
961 liquid jet fragmented by a swirled gas co-flow. *International Journal of Multiphase Flow* **152**,
962 104056.
- 963 KANDASAMY, RANJITH, HO, JIN YAO, LIU, PENGFEI, WONG, TECK NENG, TOH, KOK CHUAN & OTHERS
964 2022 Two-phase spray cooling for high ambient temperature data centers: Evaluation of system
965 performance. *Applied Energy* **305**, 117816.
- 966 KO, NWM & DAVIES, POAL 1971 The near field within the potential cone of subsonic cold jets. *Journal of*
967 *Fluid Mechanics* **50** (1), 49–78.
- 968 KUHLMAN, JOHN M 1987 Variation of entrainment in annular jets. *AIAA journal* **25** (3), 373–379.
- 969 KUMAR, ABHIJEET & SAHU, SRIKRISHNA 2019 Large scale instabilities in coaxial air-water jets with annular
970 air swirl. *Physics of Fluids* **31** (12).
- 971 KWARK, Ji-HYUN, JEONG, YONG-KI, JEON, CHUNG-HWAN & CHANG, YOUNG-JUNE 2005 Effect of swirl
972 intensity on the flow and combustion of a turbulent non-premixed flat flame. *Flow, Turbulence and*
973 *combustion* **73**, 231–257.
- 974 LALLART, ADELIN, CARTELLIER, A, GARNIER, PHILIPPE, CHARLAIX, ELISABETH & LORENCEAU, ELISE 2024
975 The fluid mechanics of spray cleaning: when the stress amplification at the contact lines of impacting
976 droplets nano-scrap particles. *Journal of Fluid Mechanics* **1000**, A31.
- 977 LASHERAS, JC, VILLERMAUX, EMMANUEL & HOPFINGER, EJ 1998 Break-up and atomization of a round
978 water jet by a high-speed annular air jet. *Journal of Fluid Mechanics* **357**, 351–379.
- 979 LASHERAS, JUAN C & HOPFINGER, EJ 2000 Liquid jet instability and atomization in a coaxial gas stream.
980 *Annual review of fluid mechanics* **32** (1), 275–308.
- 981 LAU, TIMOTHY CW & NATHAN, GRAHAM J 2014 Influence of stokes number on the velocity and concentration
982 distributions in particle-laden jets. *Journal of fluid mechanics* **757**, 432–457.
- 983 LAU, TIMOTHY CW & NATHAN, GRAHAM J 2016 The effect of stokes number on particle velocity and
984 concentration distributions in a well-characterised, turbulent, co-flowing two-phase jet. *Journal of*
985 *Fluid Mechanics* **809**, 72–110.
- 986 LAZARO, BJ & LASHERAS, JC 1992 Particle dispersion in the developing free shear layer. part 2. forced flow.
987 *Journal of Fluid Mechanics* **235**, 179–221.
- 988 LIEPMANN, DORIAN & GHARIB, MORTEZA 1992 The role of streamwise vorticity in the near-field entrainment
989 of round jets. *Journal of Fluid Mechanics* **245**, 643–668.
- 990 LING, Y, FUSTER, DANIEL, TRYGGVASON, G & ZALESKI, S 2019 A two-phase mixing layer between parallel

- 991 gas and liquid streams: multiphase turbulence statistics and influence of interfacial instability. *Journal*
992 *of Fluid Mechanics* **859**, 268–307.
- 993 LONGMIRE, ELLEN K & EATON, JOHN K 1992 Structure of a particle-laden round jet. *Journal of Fluid*
994 *Mechanics* **236**, 217–257.
- 995 LOZANO, A & BARRERAS, F 2001 Experimental study of the gas flow in an air-blasted liquid sheet.
996 *Experiments in fluids* **31** (4), 367–376.
- 997 MACHICOANE, NATHANAEL, RICARD, GUILLAUME, OSUNA-OROZCO, RODRIGO, HUCK, PETER DEARBORN
998 & ALISEDA, ALBERTO 2020 Influence of steady and oscillating swirl on the near-field spray
999 characteristics in a two-fluid coaxial atomizer. *International Journal of Multiphase Flow* **129**, 103318.
- 1000 MAKHNENKO, IAROSLAV, ALONZI, ELIZABETH R, FREDERICKS, STEVEN A, COLBY, CHRISTINE M & DUTCHER,
1001 CARI S 2021 A review of liquid sheet breakup: Perspectives from agricultural sprays. *Journal of*
1002 *Aerosol Science* **157**, 105805.
- 1003 MANISH, M & SAHU, SRIKRISHNA 2019 Droplet clustering and local spray unsteadiness in air-assisted sprays.
1004 *Experimental Thermal and Fluid Science* **100**, 89–103.
- 1005 MARMOTTANT, PHILIPPE & VILLERMAUX, EMMANUEL 2004 On spray formation. *Journal of fluid mechanics*
1006 **498**, 73–111.
- 1007 MATAS, JEAN-PHILIPPE, DELON, ANTOINE & CARTELLIER, ALAIN 2018 Shear instability of an axisymmetric
1008 air–water coaxial jet. *Journal of Fluid Mechanics* **843**, 575–600.
- 1009 MODARRESS, D, TAN, H & ELGHOBASHI, So 1984 Two-component lda measurement in a two-phase turbulent
1010 jet. *AIAA journal* **22** (5), 624–630.
- 1011 MULIADI, ARIEL & SOJKA, PAUL E 2010 A review of pharmaceutical tablet spray coating. *Atomization and*
1012 *Sprays* **20** (7).
- 1013 OBERLEITHNER, KILIAN, SIEBER, MORITZ, NAYERI, CHRISTIAN NAVID, PASCHEREIT, CHRISTIAN OLIVER,
1014 PETZ, CHRISTOPH, HEGE, H-C, NOACK, BERND R & WYGNANSKI, I 2011 Three-dimensional coherent
1015 structures in a swirling jet undergoing vortex breakdown: stability analysis and empirical mode
1016 construction. *Journal of fluid mechanics* **679**, 383–414.
- 1017 OSUNA OROZCO, RODRIGO 2021 Characterization and control of electrostatically assisted two-fluid coaxial
1018 atomization. PhD thesis.
- 1019 OSUNA-OROZCO, RODRIGO, MACHICOANE, NATHANAEL, HUCK, PETER D & ALISEDA, ALBERTO 2019 Feedback
1020 control of coaxial atomization based on the spray liquid distribution. *Atomization and Sprays* **29** (6).
- 1021 OSUNA-OROZCO, RODRIGO, MACHICOANE, NATHANAEL, HUCK, PETER D & ALISEDA, ALBERTO 2020 Feedback
1022 control of the spray liquid distribution of electrostatically assisted coaxial atomization. *Atomization*
1023 *and Sprays* **30** (1).
- 1024 OSUNA-OROZCO, RODRIGO, MACHICOANE, NATHANAEL, HUCK, PETER D & ALISEDA, ALBERTO 2022 Effect
1025 of electrostatic forcing on coaxial two-fluid atomization. *Physical Review Fluids* **7** (7), 074301.
- 1026 PANCHAPAKESAN, NAGANGUDY R & LUMLEY, JOHN L 1993 Turbulence measurements in axisymmetric jets
1027 of air and helium. part 1. air jet. *J. Fluid Mech.* **246**, 197–223.
- 1028 PARK, CJ & CHEN, L-D 1989 Experimental investigation of confined turbulent jets part 11: particle-laden
1029 flow data. *AIAA journal* **27** (11), 1511–1516.
- 1030 POPE, STEPHEN B 2001 Turbulent flows. *Measurement Science and Technology* **12** (11), 2020–2021.
- 1031 PREVOST, F, BOREE, J, NUGLISCH, HJ & CHARNAY, GEORGES 1996 Measurements of fluid/particle correlated
1032 motion in the far field of an axisymmetric jet. *International journal of multiphase flow* **22** (4),
1033 685–701.
- 1034 PRÉAUX, G, LASHERAS, JUAN CARLOS & HOPFINGER, EMIL J. 1998 Atomization of a liquid jet by a high
1035 momentum coaxial swirling gas jet. In *Proc. 3rd Int. Conf. Multiphase Flow*.
- 1036 QADDAH, BARAA, CHAPELLE, PIERRE, BELLON, JEAN PIERRE, JOURDAN, JULIEN, KEWALRAMANI, GAGAN,
1037 DEBORDE, AGATHE, HAMMES, RAPHAEL & RIMBERT, NICOLAS 2024 Primary and secondary breakup
1038 of molten ti64 in an eiga atomizer for metal powder production. *Powder Technology* **438**, 119665.
- 1039 RAJAMANICKAM, KUPPURAJ & BASU, SAPTARSHI 2017 Insights into the dynamics of spray–swirl interactions.
1040 *Journal of Fluid Mechanics* **810**, 82–126.
- 1041 RAJAMANICKAM, KUPPURAJ & BASU, SAPTARSHI 2018 Insights into the dynamics of conical breakdown
1042 modes in coaxial swirling flow field. *Journal of Fluid Mechanics* **853**, 72–110.
- 1043 REHAB, H, VILLERMAUX, E & HOPFINGER, EJ 1997 Flow regimes of large-velocity-ratio coaxial jets. *Journal*
1044 *of Fluid Mechanics* **345**, 357–381.
- 1045 ROSTAMI, ALI, LI, RI & KHEIRKHAH, SINA 2024 Three-dimensional clustering characteristics of large-stokes-
1046 number dilute sprays interacting with turbulent swirling co-flows. *Journal of Fluid Mechanics* **999**,
1047 A73.

- 1048 ROSTAMI, ALI, LI, RI & KHEIRKHAH, SINA 2025 Three-dimensional positioning, sizing, and velocimetry of
1049 dilute sprays using paired astigmatic interferometric particle imaging (paipi). *Experiments in Fluids*
1050 **66** (6), 124.
- 1051 SAHU, SRIKRISHNA & OTHERS 2018 Analysis of droplet clustering in air-assist sprays using voronoi
1052 tessellations. *Physics of Fluids* **30** (12).
- 1053 SBRIZZAI, FABIO, VERZICCO, ROBERTO, PIDRIA, MARCO F & SOLDATI, ALFREDO 2004 Mechanisms for
1054 selective radial dispersion of microparticles in the transitional region of a confined turbulent round
1055 jet. *International Journal of Multiphase Flow* **30** (11), 1389–1417.
- 1056 SHUEN, J-S, SOLOMON, ASP, ZHANG, QF & FAETH, GM 1985 Structure of particle-laden jets-measurements
1057 and predictions. *AIAA journal* **23** (3), 396–404.
- 1058 SINGH, G, JUDDO, M, KOURMATZIS, A, DUNN, MJ & MASRI, AR 2020 Heat release zones in turbulent,
1059 moderately dense spray flames of ethanol and biodiesel. *Combustion and Flame* **220**, 298–311.
- 1060 SQUIRES, KYLE D & EATON, JOHN K 1990 Particle response and turbulence modification in isotropic
1061 turbulence. *Physics of Fluids A: Fluid Dynamics* **2** (7), 1191–1203.
- 1062 TAKAHASHI, MAMORU, FUKUI, REN, TSUJIMOTO, KOICHI, ANDO, TOSHITAKE & SHAKOUCHI, TOSHIHIKO 2023
1063 Helical structures in a temporally developing round jet in the developed state. *Flow, Turbulence and*
1064 *Combustion* **111** (1), 59–79.
- 1065 TOLFTS, OLIVER, DEPLUS, GUILLAUME & MACHICOANE, NATHANAËL 2023 Statistics and dynamics of a liquid
1066 jet under fragmentation by a gas jet. *Physical Review Fluids* **8** (4), 044304.
- 1067 TOLFTS, OLIVER, RACK, ALEXANDER & MACHICOANE, NATHANAËL 2024 Morphology and dynamics of the
1068 liquid jet in high-speed gas-assisted atomization retrieved through synchrotron-based high-speed
1069 x-ray imaging. *International Journal of Multiphase Flow* **181**, 105004.
- 1070 TRATNIG, ANDREAS & BRENN, GÜNTER 2010 Drop size spectra in sprays from pressure-swirl atomizers.
1071 *International Journal of Multiphase Flow* **36** (5), 349–363.
- 1072 TSO, JIN & HUSSAIN, FAZLE 1989 Organized motions in a fully developed turbulent axisymmetric jet. *Journal*
1073 *of Fluid Mechanics* **203**, 425–448.
- 1074 ÜNAL, A 1989 Liquid break-up in gas atomization of fine aluminum powders. *Metallurgical Transactions B*
1075 **20**, 61–69.
- 1076 WU, HAO, ZHANG, FUJUN, ZHANG, ZHENYU & HOU, LIN 2022 Atomization and droplet dynamics of a gas-
1077 liquid two-phase jet under different mass loading ratios. *International Journal of Multiphase Flow*
1078 **151**, 104043.
- 1079 YARIN, ALEXANDER L, ROISMAN, ILIA V & TROPEA, CAMERON 2017 *Collision phenomena in liquids and*
1080 *solids*. Cambridge University Press.
- 1081 YODA, M, HESSELINK, L & MUNGAL, MG 1992 The evolution and nature of large-scale structures in the
1082 turbulent jet. *Physics of Fluids A: Fluid Dynamics* **4** (4), 803–811.
- 1083 ZANDIAN, ARASH, SIRIGNANO, WILLIAM A & HUSSAIN, FAZLE 2018 Understanding liquid-jet atomization
1084 cascades via vortex dynamics. *Journal of Fluid Mechanics* **843**, 293–354.
- 1085 ZHOU, HUA, HAWKES, EVATT R, LAU, TIMOTHY CW, CHIN, REY, NATHAN, GRAHAM J & WANG, HAIYOU 2022
1086 Understanding of turbulence modulation and particle response in a particle-laden jet from direct
1087 numerical simulations. *Journal of Fluid Mechanics* **950**, A3.